

RESEARCH ARTICLE

10.1029/2018MS001390

Convectively Generated Gravity Waves in High Resolution Models of Tropical Dynamics

Key Points:

- The zonal wave number spectrum of stratospheric zonal momentum flux is $\sim k^{-1}$
- Gravity wave momentum flux is weakened substantially when coarsening horizontal grid spacing and by a parameterization of convection
- In realistic simulations of tropical dynamics the universal properties of gravity wave spectra are fulfilled

Correspondence to:

S. K. Müller, sebastian.mueller@mpimet.mpg.de

Citation:

Müller, S. K., Manzini, E., Giorgetta, M. A., Sato, K., & Nasuno, T. (2018). Convectively generated gravity waves in high resolution models of tropical dynamics. *Journal of Advances in Modeling Earth Systems*, 10, 2564–2588. <https://doi.org/10.1029/2018MS001390>

Received 29 MAY 2018

Accepted 3 OCT 2018

Accepted article online 5 OCT 2018

Published online 27 OCT 2018

Sebastian K. Müller¹, Elisa Manzini¹, Marco Giorgetta¹, Kaoru Sato², and Tomoe Nasuno³

¹Max Planck Institute for Meteorology, Hamburg, Germany, ²Department of Earth and Planetary Science, University of Tokyo, Japan, ³Japan Agency for Marine Earth Science and Technology, Yokosuka, Japan

Abstract We investigate numerical models that display the transition of global climate modeling from coarse grids, at which convection and gravity waves are still parameterized, toward finer resolutions, where both are treated explicitly. Gravity waves generated by deep, tropical convection are examined by means of spectral analysis. We make use of the models' different setups to discuss the impacts of spatial resolution, the treatment of moist convection and the degree of model complexity, on convectively generated gravity waves. We find that substantially more gravity wave momentum flux is resolved by models with fine horizontal grid spacing, as the spectral slope is almost flat in zonal wave number space ($\sim k^{-1}$), until scales at which numerical diffusion sets in. However, we also find that, when well-organized tropical storm systems of large scale are simulated with convection-permitting resolution, the gravity wave variance may be enhanced at small scales and the spectral slope may flatten. We propose an explanation for this in the dynamical overshooting of convective updrafts that is expected to mechanically generate gravity waves. Further, we find that a parameterization of convection drastically reduces gravity wave momentum flux associated with tropical convection, as deep modes of latent heating and gravity waves are underestimated. Thus, its application is expected to have consequences for wave mean-flow interaction in the middle atmosphere. The universal properties of the gravity wave spectrum that were found in observations and confirmed in analytical gravity wave models are successfully reproduced in our numerical simulations of tropical dynamics.

1. Introduction

In the tropics deep convection is the primary source of atmospheric gravity waves and these convectively generated gravity waves (CGGWs) contribute significantly to the stratospheric momentum budget (Fritts & Alexander, 2003). Alexander and Holton (1997) and Piani et al. (2000) showed in numerical model studies of tropical deep convection that the small-scale gravity waves excited by deep convection can contribute significantly to the wave forcing necessary for driving the quasi-biennial oscillation (QBO; Baldwin et al., 2001). Sato and Dunkerton (1997) confirmed with observations that the momentum flux associated with gravity waves is much larger than those of Kelvin waves and Rossby-gravity waves. In this study we investigate CGGWs with wavelengths of 10 to 1,000 km, by means of numerical models of tropical dynamics, and assess their sensitivity to spatial resolutions and model configurations. Convectively triggered gravity waves can hardly be resolved in current climate models and to this end (nonorographic) gravity wave parameterizations, accounting for underlying convective activity in the tropics, were introduced (Beres et al., 2005; Orr et al., 2010; Richter et al., 2010, e.g.). Here we explore how the explicit treatment of both, convection and its gravity waves, will impact both their statistical and spectral properties. In doing so we can in advance assess how the convection-gravity wave links are realized in future generations of high-resolution climate models.

The properties of atmospheric internal gravity waves were first described in observational studies (e.g., Sato, 1992; Smith et al., 1985; Tsuda et al., 1989, 1994), using lidar and radar to obtain vertical profiles of wind and temperature fluctuations. Universal properties of the power spectral densities were found analogously to gravity waves in the ocean (Garrett & Munk, 1972, 1975). These findings inspired theories, based upon analytical gravity wave models, for their explanation (e.g., Dewan & Good, 1986; Hines, 1991; Sato & Yamada, 1994; Smith et al., 1987; Warner & McIntyre, 1996; Weinstock, 1985a). The properties of gravity wave spectra, in vertical and horizontal wave number and in frequency space, are summarized in Gardner et al. (1993).

©2018. The Authors.

This is an open access article under the terms of the Creative Commons Attribution-NonCommercial-NoDerivs License, which permits use and distribution in any medium, provided the original work is properly cited, the use is non-commercial and no modifications or adaptations are made.

In this paper we present an extensive test of modern atmospheric models in reproducing the universal spectral properties of gravity waves.

Convective clouds generate gravity waves in the first place as a consequence of the release of latent heat. This mechanism is referred to as thermal forcing (Fritts & Alexander, 2003) and is used for parameterizations of CGGWs. In linearized models (e.g., Holton, 1973; Salby & Garcia, 1987) it was found that the latent heating profile in convective storms controls properties of the generated waves. Through the doubling of buoyancy frequency from the troposphere to the stratosphere the dominant vertical wavelength is expected to be equal to twice the vertical depth of the heating. This relation has been confirmed in observations (McLandress et al., 2000) and numerical modeling studies (Alexander et al., 1995). Still, as shown in Holton et al. (2002), the response of gravity waves to a diabatic heat source is complex and involves all spatial and temporal scales of diabatic heating.

Along with the thermal forcing mechanism, also two other convective gravity wave generation mechanisms, referred to as mechanical oscillation and transient mountain effect (Fritts & Alexander, 2003), have been discussed. T. L. Clark et al. (1986) describe the excitation of gravity waves through the oscillation of convective updrafts below a stably stratified layer. This mechanism was confirmed in numerical model studies of squall lines by Fovell et al. (1992) and Alexander et al. (1995). It is challenging to disentangle the generation mechanisms, as latent heating and vertical motion in convective clouds are intrinsically coupled. By means of a gravity wave source term analysis applied to a numerical model simulation of maritime sea-breeze convection, Lane et al. (2001) found that for these conditions the mechanical oscillator effect is the dominant convective gravity wave generation mechanism. However, in a related study, Song et al. (2003) showed that the mechanical generation is less efficient, as it is confined by the vertical propagation condition, and that the effectivity of mechanical (nonlinear) and thermal (diabatic) forcing are of comparable magnitudes. The transient mountain effect only comes into play when there is flow across a convective cloud's top. Within the cloud latent heating lowers the potential temperature surface and air parcels flowing along the surface are displaced vertically as in flow over orography.

In the last two decades numerical, cloud-resolving model simulations became a leading tool in research on CGGWs. Lane and Moncrieff (2008) describe characteristics of horizontal wave number and frequency spectra, in particular three dominant modes of the wave spectrum. They use a model solving nonhydrostatic anelastic equations of motion (see L. Clark et al., 1996) for idealized simulations of tropical convection with similar, although two-dimensional, domain size and grid spacing as our high-resolution simulations and as such their study constitutes an important reference. Piani et al. (2000), Piani and Durran (2001), and Beres et al. (2002) used 3-D models of squall lines and focused on the wave mean-flow interaction of CGGWs, that contributes to the QBO and mesospheric QBO. Another motivation concerns the representation of gravity waves in a numerical model itself, with Lane and Knivvel (2005) and Watanabe et al. (2015) investigating the dependency of the gravity wave fields on spatial resolution and Stephan and Alexander (2014) on microphysical parameterizations. While the horizontal as well as the vertical grid spacing have a strong impact on the spectral characteristics and absolute momentum flux of gravity waves, microphysical parameterizations were shown to have little influence on gravity wave characteristics.

Along with continuously increasing computational resources, mesoscale-resolving general circulation models have become feasible. Liu et al. (2014), using a 0.25° -horizontal-resolution model, reveal that gravity waves become increasingly dominant with altitude and find a flattening of the slope of horizontal wave number spectra of kinetic energy with altitude. Holt et al. (2016) used 2-year simulations with a General Circulation Model (GCM) at 7-km-horizontal resolution to investigate tropical waves and the QBO. They found in their simulation, which still employed a parameterization of convection, that the zonal wave forcing is still too low and a gravity wave parameterization is still needed to drive a QBO-like oscillation. These results raise questions on how spatial resolution impacts the stratospheric wave forcing in a general circulation model and can still not estimate the numerical resolution at which gravity wave drag parameterizations become obsolete.

In this paper we explore convection and gravity waves in a range of numerical models of tropical dynamics. We built a model of idealized tropical dynamics, using a spherical domain, with a radius of an eighth of the Earth's. The high-resolution version has a horizontal grid spacing of 2.5 km, with the potential of resolving deep convection. As the following analysis indeed confirms that this model simulates deep convection it fits into the class of *deep convection-permitting* models (Prein et al., 2015). We also use a coarse-resolution version, with a grid spacing of 20 km, which we investigate in two simulations—one with and the other without

the use of a parameterization of convection. In addition, we analyze two numerical simulations in realistic boundary conditions of the tropical atmosphere, considering planetary rotation. One is a general circulation model, where we focus on the Pacific, and the other is a numerical weather prediction model, also at deep convection-permitting resolution. In contrast to previous model studies, that mostly investigated a single convective event (Alexander et al., 1995; Fovell et al., 1992; Lane et al., 2001, ...), we here cover a great variety in scales of tropical dynamics and convective systems. Thus, this study investigates CGGWs on novel spatial (three-dimensional) and temporal scales.

The specific setups of the models and the methodology of spectral analysis and cloud statistics are described in section 2. In section 3 we describe the models' representation of tropical circulations and convection. In section 4 we present results on the spectral characteristics of gravity waves in our models. Finally we discuss these results in section 5 and summarize conclusions in section 6.

2. Methods

2.1. Numerical Models and Simulations

We use the ICOSahedral Nonhydrostatic atmosphere model (ICON; Zängl et al., 2015), a joint development by MPI-M and the German weather service (DWD), in a version using physical parameterizations inherited from them ECHAM6 model (Stevens et al., 2013). Further, we investigate a simulation performed with the Nonhydrostatic ICOSahedral Atmospheric Model (NICAM, Satoh et al., 2008, Satoh et al., 2014), jointly developed at the Japan Agency for Marine–Earth Science and Technology, the Atmosphere and Ocean Research Institute, the University of Tokyo, and the RIKEN Advanced Institute for Computational Science, in Japan. Both, ICON and NICAM, use icosahedral grids and a nonhydrostatic dynamical core and are capable of performing simulations on a large variety of grids.

2.1.1. ICON—Spherical Limited Area Model

We constructed a Spherical Limited Area Model (SLAM) using ICON to provide an idealized test case of tropical dynamics. The parameterizations used for radiation, surface fluxes, turbulent diffusion, and cloud microphysics are adopted from ECHAM6 (Stevens et al., 2013). In ICON's dynamical core horizontal diffusion is realized with a flow-dependent second-order Smagorinsky diffusion of velocity and potential temperature in combination with a background fourth-order Laplacian diffusion of velocity. In addition, the dynamical core contains a fourth-order divergence damping term for numerical stability. The domain of ICON-SLAM is a sphere with a scalable radius. By the choice of this scaling the domain area and, in combination with the choice of model grid, the grid spacing are controlled. A similar modeling approach has been undertaken by Reed and Medeiros (2016). They used a range of scaling factors (from 1 to 1/16) and by that outlined the transition from global simulations of Radiative–Convective Equilibrium (RCE) toward convection-permitting simulations of RCE. For our study we aimed to simulate tropical convection up to its largest characteristic scales, given by large-scale circulations such as the Hadley Cell. Thus, we chose the radius to be an eighth of the Earth's, resulting in a circumference of 5,004 km and an area of $\sim 8 \times 10^6$ km². The bottom boundary contains no orography and only water at fixed (sea) surface temperatures (SSTs), with the profile *qobs*, designed for Aqua Planet Simulations (Neale & Hoskins, 2000a, 2000b). The ozone profile used is that suggested for the Aqua Planet Experiment (see http://www.met.reading.ac.uk/~mike/APE/ape_ozone.html). We use the initialization following the Jablonowski–Williamson test case, but set zonal wind speeds to zero, as westerly jets are not of interest.

There is no planetary rotation and thus there are no baroclinic or equatorial waves. We use a zonally symmetric but meridionally varying solar insolation, which pulsates with a diurnal cycle. In this way, we constructed a zonally symmetric, idealized model of tropical dynamics.

We performed three simulations using ICON-SLAM, that was introduced in Chapter SLAM. The hiSLAM was conducted on an icosahedral grid with 1,310,720 cells and 2.5 km nominal grid spacing, a resolution typical for deep convection-permitting models (Prein et al., 2015). The other two simulations were performed on a grid of 20,480 cells with 20 km nominal grid spacing (coSLAMs), one of them (coSLAM-pc) with the use of the Nordeng cumulus convection parameterization scheme (Nordeng, 1994), the other without (coSLAM-xc). All simulations share a stretched, vertical grid with 95 levels and the model top is at 83 km. Also, the integration time step is equal for all experiments and set to 20 s. Rayleigh damping Klemp et al. (2008) is applied for the levels in between 50 and 83 km height for preventing wave reflection at the model top. The output frequency is 15 min for 3-D variables and 5 min for 2-D variables. The integration period is 90 days for hiSLAM and 150 days for coSLAMs. For spectral analyses we interpolated the model output onto Gaussian grids, with grid spacings of 4.88 and 39.1 km at the Equator, for hiSLAM and coSLAMs, respectively.

Table 1
Model Overview

Model	Simulation name	Grid spacing (km)	Vertical levels	Model top (km)	Integration period (day)	Output frequency 3-D (min)/2-D (min)	Parameterization of convection
ICON	hiSLAM	2.5	95	83	90	15/5	No
ICON	coSLAM-xc	20	95	83	150	15/5	No
ICON	coSLAM-pc	20	95	83	150	15/5	Yes
NICAM	ICSOM1	14	128	38	7	15/15	No
ICON	NARVAL2	2.5	75	30	30 × 1	60/30	No

Note. ICON = ICOSahedral Non-Hydrostatic atmosphere model; SLAM = Spherical Limited Area Model; NICAM = Nonhydrostatic ICOSahedral Atmospheric Model.

2.1.2. NICAM - ICSOM1

For the Interhemispheric Coupling Study by Observations and Modeling (ICSOM, see <http://pansy.eps.s.u-tokyo.ac.jp/icsom/>) a combination of observations and NICAM model simulations is used. The simulation investigated here is performed on a global domain, defined on a icosahedral mesh with 14-km grid spacing, and covers the time period from 31 January 2016 to 06 February 2016 0000 UTC. The vertical grid consists of 128 levels and the model top is at 38 km. Moist processes are explicitly calculated using a single-moment bulk cloud microphysics scheme (Tomita, 2008), and no cumulus convection parameterization scheme is used. In NICAM's dynamical core, as used for the ICSOM1 simulation, there are two kinds of numerical diffusion schemes (linear and nonlinear) used to handle computational instability (Satoh et al., 2008). These diffusion operators also efficiently damp waves toward the model top and no explicit *sponge layer* is required. The Mellor-Yamada-Nakanishi-Niino level-2 turbulent scheme (Mellor & Yamada, 1982; Nakanishi & Niino, 2006; Noda et al., 2010) is applied as a parameterization of atmospheric turbulent processes. The model atmosphere was initialized using interpolated ERA-Interim data and SSTs were given by an interpolation of NCEP final analyses surface temperature. The simulation was run on the Earth Simulator at JAMSTEC. The analyses presented in this paper focus on a region covering the tropical Pacific, from 120°E to 80°W and from 30°S to 30°N (number of grid points: $1,138 \times 426 = 484,788$, area covered: $17,791 \times 6671 \text{ km} = 119 \times 10^6 \text{ km}^2$). All variables are output every 15 min.

2.1.3. ICON—NARVAL2

For the NARVAL2 campaign a wide range of airborne and ground-based measurements were taken and complemented with high-resolution numerical model simulations, using ICON (see also Klocke et al., 2017).

Different to ICON-SLAM simulations, the DWD physics package is used, with parameterizations of radiative transfer, subgrid scale orography and microphysics. There is no parameterization of convection or nonographic gravity waves in use. While SLAMs and NARVAL2 share the diffusion schemes of their common dynamical core, unresolved turbulent fluxes are parameterized differently. For NARVAL2 the turbulence parameterization is similar to the level-2.5 scheme of Mellor and Yamada (1982) and described in Baldauf et al. (2011). We analyze simulations on a domain covering the tropical Atlantic from 15°E to 68°W and from 10°S to 20°N and an area of $\sim 31 \times 10^6 \text{ km}^2$. The model's horizontal grid consists of 4,887,488 cells with a grid spacing of 2.5 km. The remap of the model grid, that we use for spectral analysis, has $3,281 \times 1,161 = 3,809,241$ points. The vertical grid consists of 75 levels and the model top is at 30 km. The Rayleigh damping scheme is here applied for levels above 25 km altitude. The integration period, matching that of the observations, starts 26 July 2016 and ends 31 August 2016. The 3-D variables are output 1-hourly and 2-D variables half-hourly. At each day the simulation was reinitialized with European Centre for Medium-Range Weather Forecasts (ECMWF) forecasts and integrated for 36 hr. Lateral boundary conditions and SSTs origin also from ECMWF and are updated every 3 hr. We neglect the first 12 hr of each simulation to omit numerical artifacts arising from the interpolation at initialization.

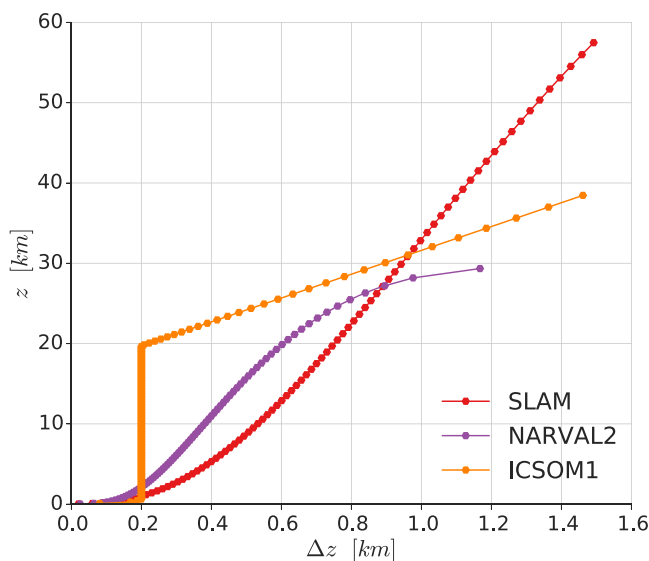


Figure 1. Vertical grid spacing, Δz , with height z . SLAM = Spherical Limited Area Model; ICSOM = Interhemispheric Coupling Study by Observations and Modeling.

Table 2
Time Periods Used for Cloud Statistics and Spectral Analyses

Simulation	Cloud statistics— Figures 6, 7, and 8	Zonal wave number spectra— Figures 9 and 10 (days)	Wave number-frequency spectra— Figure 11 (days/chunks)	Frequency spectra— Figure 10 (days)
hiSLAM	271 time steps	[20;90]	[20;90]/10	[20;90]
coSLAM-xc	1098 time steps	[10;150]	[10;150]/20	[20;150]
coSLAM-pc	1098 time steps	[10;150]	[10;150]/20	[20;150]
ICSOM1	-	[0;6]	[0;6]/0	[0;6]
NARVAL2	72 time steps	[0;30]	[0;30]/4	[0;30]

Note. SLAM = Spherical Limited Area Model; ICSOM = Interhemispheric Coupling Study by Observations and Modeling.

2.1.4. Model Summary

For our study of CGGWs we use high-resolution models (hiSLAM and NARVAL2) and compare them to models with coarser resolutions (coSLAMs and ICSOM1). Also, we are also able to analyze the impacts of a parameterization of convection, when comparing coSLAM-xc and coSLAM-pc. The idealized SLAM experiments serve to analyze the convection and CGGWs in simplified circumstances, compared to convection and CGGWs in the realistic and more complex circumstances of NARVAL2 and ICSOM1. None of the simulations uses a gravity wave drag parameterization. All simulations studied herein are summarized in Table 1. Figure 1 shows the vertical resolution in the different simulations.

2.2. Statistical Analysis of Clouds

In section 3.2 we discuss probability distributions of vertical velocity w_{cld} , perturbation temperature T'_{cld} , and latent heating rate Q_{lat} for samples of cloudy grid cells. At any height, a grid cell is defined to be cloudy if its total cloud condensate mass mixing ratio q_T is greater than 0.1 g/kg.

The perturbation temperature in a cloudy grid cell with a horizontal coordinate c at a given height z and time t is computed as

$$T'_{\text{cld}}(c, z, t) = T_{\text{cld}}(c, z, t) - \bar{T}(z), \quad (1)$$

with $\bar{T}(z)$ denoting the mean at level z over all grid cells and over time.

The probabilities presented in Figures 6, 7, and 8 are computed through binning the respective quantity as for a histogram, with a normalization given through the absolute number of cloudy cells of each level. Thus, the sum of each level's probabilities equals 1 (100%). The bin size is the same for all simulations: 0.1 m/s for w_{cld} , $\frac{1}{3}$ K for T'_{cld} , and $\frac{1}{3} \cdot 10^{-3} \text{Ks}^{-1}$ for Q_{lat} . The bin size in the vertical is 150 m, given by an interpolation from the stretched vertical grid of the model onto a uniform vertical grid.

To the probability distribution we add the mean vertical profile. Further, we show the temporal means of the 10th and 90th percentiles, and of the minima and maxima, of each level. Their respective spreads give an estimate of the quantity's variability within a cloud.

2.3. Spectral Analysis

We investigate gravity wave characteristics by means of spectral analysis. The spectral power P estimates the variance of a variable, like vertical velocity $w(x, t)$ (x being the zonal coordinate and t being time), in spectral space of zonal wave number k (or zonal wavelength λ) and frequency ω . It is given by the product of the discrete Fourier transform $F_w(k, \omega)$ of w with its complex conjugate $F_w^*(k, \omega)$. In general, it reads as

$$P_{ww}(k, \omega) = F_w(k, \omega)F_w^*(k, \omega). \quad (2)$$

For a covariant property, like zonal momentum flux uw , we compute the cross-spectral power, which is given by the real part (denoted with Re) of the product of the Fourier transform of u times the complex conjugate of the Fourier transform of w :

$$P_{uw}(k, \omega) = \text{Re}(F_u(k, \omega)F_w^*(k, \omega)). \quad (3)$$

The finite character of our time series and noncyclic lateral boundaries (NARVAL2 and ICSOM1) introduce biases to the periodogram. These we reduce with a split-cosine taper, covering an eighth of each side of the

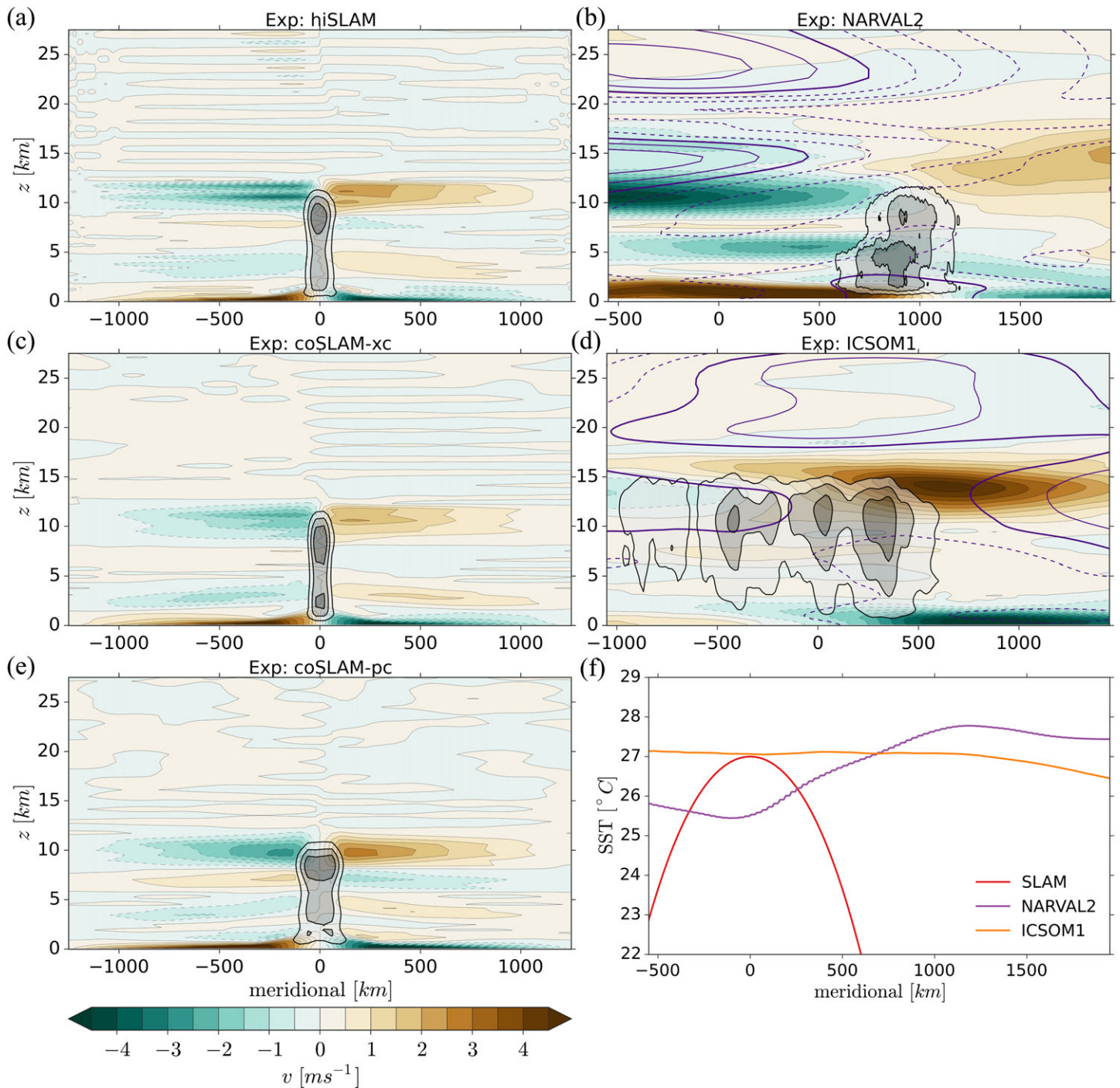


Figure 2. Panels (a)–(e): Temporal and zonal mean of the meridional wind, v [m/s], in colored shading, and of the zonal wind indicated by purple and vertical velocity indicated by black contours. For zonal wind, the thick solid contour indicates the zero-line, the contour interval is 5 m/s and negative values are dashed. For SLAMs this is omitted as there is no zonal circulation. The horizontal axis shows the distance in kilometer from pole to pole, with 0 denoting the Equator in NARVAL2 and ICSOM1, and the central parallel for SLAMs. For NARVAL2 only the central part of the Atlantic, from 45 to 20°W is considered. For vertical velocity the three contours refer to one, two, and three quarter's of the simulation's maximum vertical velocity. The maxima have magnitudes of 0.08 m/s for hiSLAM, 0.02 m/s for NARVAL2, 0.08 m/s for coSLAM-xc, 0.03 m/s for ICSOM1, and 0.06 m/s for coSLAM-pc. Panel (f) shows the temporal and zonal mean of SST. For all simulations the temporal means are taken over the whole integration period. SLAM = Spherical Limited Area Model; ICSOM = Interhemispheric Coupling Study by Observations and Modeling; SST = sea surface temperature.

time series, as well as of the zonal dimension. To reduce the uncertainty of the periodogram in time, we smooth the spectra using the *Chunk Spectral Estimator*, that is, subdividing the time series into subsamples, so-called chunks, and taking their average. Further, the chunks are overlapping by half of their length, meaning that we use every time step in our spectral analysis twice. Along with the time periods used for spectral analyses, the number of chunks used is given in Table 2. We average all spectra over zonal bands, ranging from 10°S to 10°N for SLAMs and ICSOM1, and from 5°N to 15°N for NARVAL2, accounting for the location of the Intertropical Convergence Zone (ITCZ). Thus, the spectra are averaged over eight parallels for coSLAMs, over 58 for hiSLAM, over 142 for ICSOM1, and over 400 for NARVAL2. Note that the scaling applied to the radius of SLAMs means also a reduction of the meridional length in SLAMs, when compared to NARVAL2 and ICSOM1. The meridional variation of the circumference is considered through multiplying the spectrum of each zonal band by the cosine of latitude.

Applying the spectral analysis in the region above convection at 20 km altitude aims at revealing the *near-field* characteristics of the gravity wave field. Additionally for SLAMs, we compute spectra also in meridional wave number space, that is, along each meridian and from pole to pole, with a zonal and temporal average. Tapering and weighting for the reduction of the grid cell area toward the poles is done by the multiplication of the variable by the cosine of latitude. With that approach the whole domain is considered and thus we refer to those spectra as *global*.

The wave number-frequency spectra presented in section 4.2 are computed from two-dimensional discrete Fourier Transforms, following equation (3). They are normalized for the simulations' respective maximum value, as we are interested in their characteristics in a qualitative sense.

For testing the gravity wave spectra for their universal properties we use one-dimensional spectra, in zonal wave number and frequency space (section 4.1) as well as in vertical wave number space (section 4.3). The one-dimensional discrete Fourier Transforms are computed, either in the zonal dimension, with an average over time, for a zonal wave number spectrum, or in time with an average over all zonal grid points, for a frequency spectrum. For spectra of zonal momentum flux uw , we take the absolute value of the cross-spectral power, as it can take negative values. We then compute the power spectral density, p , accounting for the sample length in space/time and its resolution, as well as for the mean air density at the respective altitude.

For spectra in vertical wave number space we interpolated the model output onto a linearly spaced vertical grid (from 15 to 55 km for SLAMs to 27.5 km for NARVAL2 and 38 km for ICSOM1), which then allows for the computation of Fourier transforms. The noncyclic character of the vertical profile requires tapering and the three smallest wave number, due to their biases, are excluded. Also an average is taken over a large sample of columns. The normalization for power spectral density is equivalent to that of the other one-dimensional spectra.

3. Tropical Dynamics and Convection

In this section we describe the general characteristics of convection and dynamics of the simulations. In subsection 3.1 we describe their mean states, as well as characteristics of circulations and convective activity. For interpreting differences in the models' representation of convective clouds, the statistics of cloud vertical velocities, temperature perturbations, and latent heating rates are analyzed in subsection 3.2. For estimating the thermal forcing of CGGWs and relating that to spectra of gravity wave properties in the stratosphere (section 4), we present a spectral analysis of precipitation flux and upper tropospheric vertical velocity and kinetic energy in subsection 3.3.

3.1. Circulation, Clouds, and Moisture

Figure 2 shows the temporal and zonal means of the meridional and zonal wind, as well as of vertical velocities. The temporal and zonal means of SSTs are shown in Figure 2f. For SLAMs they peak sharply at the central parallel and force deep convection there. This drives a thermally direct, overturning meridional circulation, with ascent only around the central parallel and subsidence, along with radiative cooling, toward higher latitudes. Consistent with that, a low-level convergence zone occurs along the central parallel. No zonal circulation is present in SLAMs, as planetary rotation is absent.

In ICSOM1 and NARVAL2 circulations are more complex and not symmetrical. There is stronger meridional low-level inflow from the winter hemisphere, whereas convection is more active in the summer hemisphere. In ICSOM1 and NARVAL2 an easterly trade wind regime and a zonal circulation in the stratosphere, associated

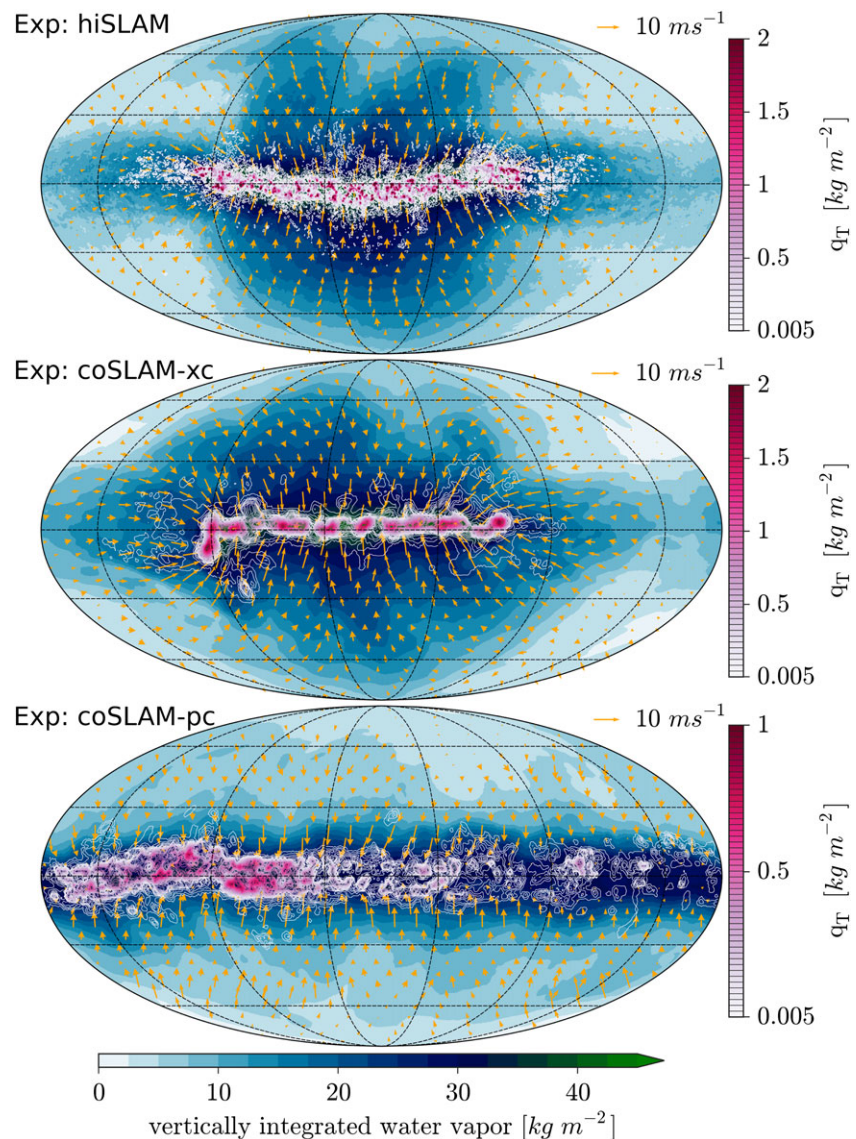


Figure 3. Full domain snapshots of SLAMs at their last integration time step: Vertically integrated water vapor [kg/m^2] is shown blueish filled contours, vertically integrated total cloud condensate is illustrated in white-to-pink contours with a linear spacing from 0.005 to 2 kg/m^2 for hiSLAM and coSLAM-xc and to 1 kg/m^2 for coSLAM-pc. Orange arrows represent surface wind vectors.

with the QBO, can be identified. The vertical velocity contours, representing vertical motion forced through convective clouds, indicate that convection is reaching higher altitudes in ICSOM1 and NARVAL2 than in SLAM simulations.

Figures 3 and 4 show snapshots of the distribution of moisture and clouds, as well as of the surface wind field, taken at the simulations' last time step. They illustrate the cloud fields of the convergence zone and the low-level flow. In hiSLAM and coSLAM-xc, where convection is treated explicitly, the convergence zone is broken up and the clouds aggregate zonally. The large-scale circulation is thus not solely given through the meridional cell, but also a zonal component of low-level inflow at the central parallel is found. This behavior is not found in coSLAM-pc, where high moisture and convection is present all along the central parallel. From this we conclude that a parameterization of convection inhibits convective self-aggregation, a result in line with Becker et al. (2017).

In ICSOM1 and NARVAL2 the ITCZ forms along the line of meridional air mass and moisture convergence and manifests in convective cloud systems of large scales in the zonal dimension. In ICSOM1 and NARVAL2

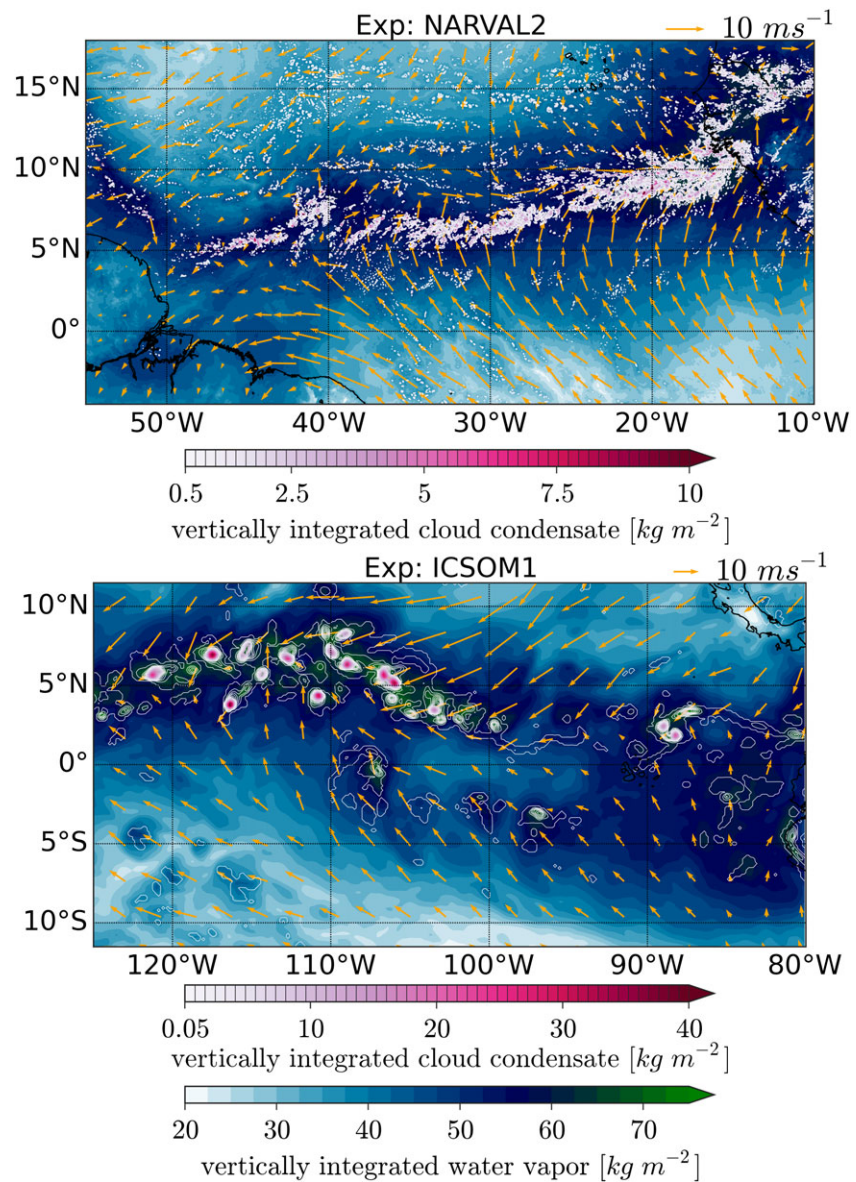


Figure 4. Like Figure 3, but for experiments NARVAL2 and ICSOM1. The plotted areas are chosen such that their zonal and meridional extents are equal to Spherical Limited Area Model's circumference and to its distance from pole to pole. The contours of vertically integrated total cloud condensate are linearly spaced from 0.5 to 10 kg/m² for NARVAL2 and from 0.05 to 40 kg/m² for ICSOM1. ICSOM = Interhemispheric Coupling Study by Observations and Modeling.

vertically integrated water vapor and cloud water condensate are notably higher, indicating a sensitivity to cloud microphysical parameterization.

Figure 5a shows cloud cover as a function of height for SLAMs and NARVAL2. It is computed as the sum of the area of cloudy cells of each level, divided by the area of columns that contain at least one cloudy grid cell. A grid cell is defined to be cloudy, if $q_T > 0.1$ g/kg. In all models the three modes of tropical convection (Johnson et al., 1999), shallow, congestus, and deep convection are present. Still the models are different with respect to each other. SLAMs show two peaks at low levels below 4 km, with similar altitudes, making it hard to distinguish shallow and congestus clouds. In coSLAM-pc deep convection's anvil clouds can be identified as a sharp peak in cloud fraction at an altitude of 8 km. In hiSLAM and coSLAM-xc this peak occurs at a higher altitude and is smoother, indicating greater variability in deep convection's cloud depth. hiSLAM and coSLAM-xc have very similar profiles, suggesting that spatial resolution, in the range of 2.5 to 20 km, does not matter for the vertical structure of tropical, convective clouds.

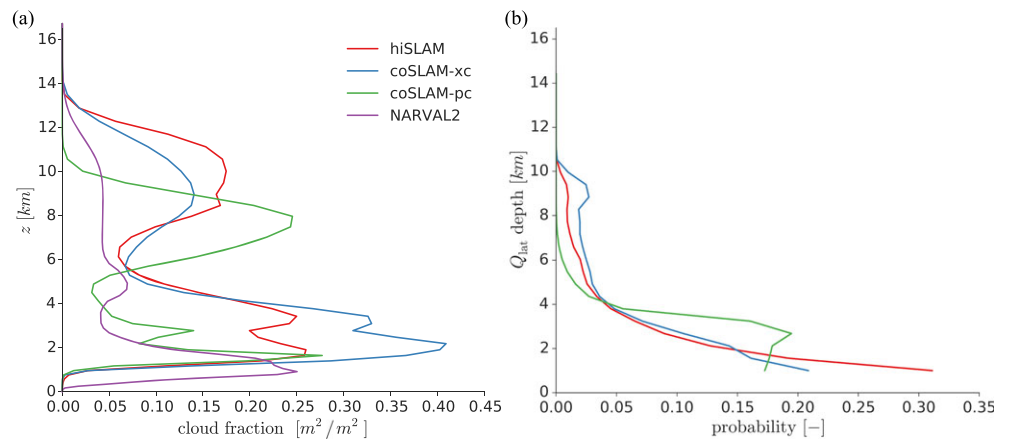


Figure 5. (a) Mean vertical profile of cloud fraction and (b) the probability distribution of the latent heating depth. Note that cloud condensate was only available for SLAMs and NARVAL2, and latent heating rate only for SLAMs. SLAM = Spherical Limited Area Model.

In NARVAL2 shallow and congestus clouds are clearly separated, with peaks in cloud fraction at ~ 1.5 and 5 km. There is no clear peak for deep convection's anvil clouds but a significant amount of cloud fraction reaches up to ~ 14 km, confirming the presence of deep convective clouds. We find that the models with explicit convection exceed coSLAM-pc in cloud top height significantly, by about 2 km, suggesting that the depth of deep convection is reduced through the use of a parameterization.

3.2. Cloud Statistics

We here characterize the models' representation of convective clouds through a statistical analysis of their dynamic and thermodynamic properties, following the methodology described in subsection 2.2. In-cloud vertical velocity w_{cld} , perturbation temperature T'_{cld} , and latent heating rate Q_{lat} are analyzed. These properties do not only characterize convective clouds themselves but also relate to their mechanical (w_{cld}) and thermal (T'_{cld} and Q_{lat}) forcing of gravity waves.

For the cloud statistics of SLAMs we presample the model output for grid cells in between 10° north and south of the central parallel. For NARVAL2 we compute cloud statistics only for the central part of the Atlantic ITCZ, from 35 to 16.5°W , and over ocean only. We miss the variables of cloud condensate for ICSOM1, so we could not compute its cloud statistics.

3.2.1. Vertical Velocity

Figure 6 shows the probability distribution of w_{cld} for all heights, computed over several time steps.

In numerical models of explicit convection the vertical motions in convective clouds, updrafts and downdrafts, are affected by the horizontal grid spacing. We see this from the differences in magnitude of w_{cld} among the high-resolution models hiSLAM and NARVAL2 and low-resolution model coSLAM-xc. Nevertheless, these three models agree on a peak in magnitude of w_{cld} at high levels above 10 km, due to latent heat release by freezing, accelerating updraft speeds still above the freezing level. In these models with explicit convection there are negative magnitudes of w_{cld} present above ~ 9 km. These reflect the oscillation of cloudy air mass around their level of neutral buoyancy, which can be interpreted as evidence for mechanical gravity wave generation. Only coSLAM-pc shows exclusively positive w_{cld} around the cloud top. The parameterization of convection parameterizes the overshooting of convective clouds beyond their level of neutral buoyancy and thus does not explicitly simulate the dynamical *overshooting* of updrafts, along with the oscillation around it. As a consequence the mechanical generation of gravity waves is expected to be inhibited by a parameterization of convection.

At lower levels negative magnitudes of w_{cld} relate to downdrafts, driven by evaporative cooling of precipitation. While hiSLAM has greater updraft velocities, downdrafts are more intense in NARVAL2.

In Figure 6e the 50th, 90th, and 99th percentiles of each time step at each level are shown for hiSLAM. A similar analysis was done by Khairoutdinov et al. (2009), who used a Large-Eddy-Simulation of tropical convection with a horizontal grid spacing of 100 m, also in a nonrotating framework. The statistics of hiSLAM compare well with the average updraft speeds shown in Figure 8b of Khairoutdinov et al. (2009), both in their structure

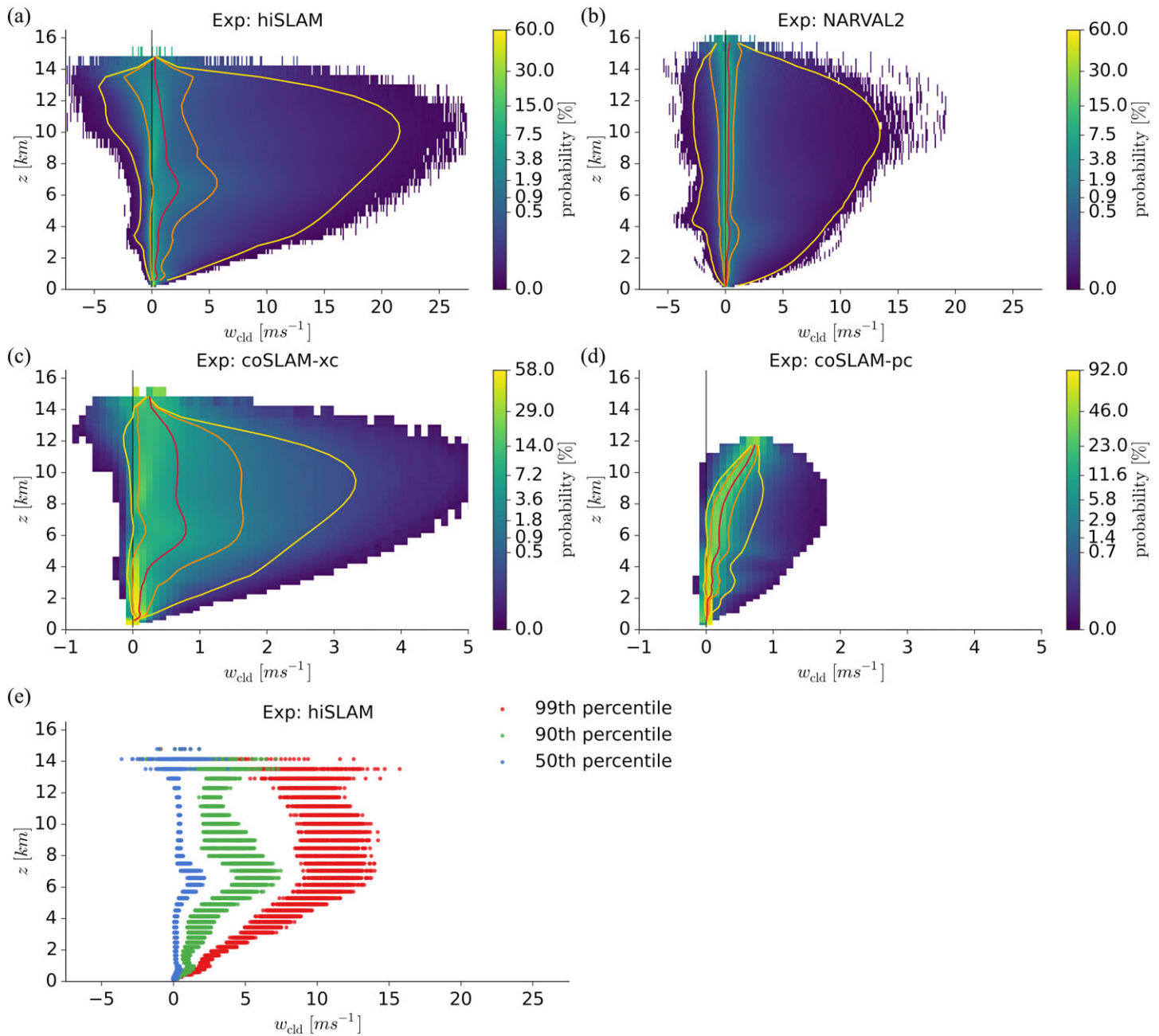


Figure 6. Panels (a)–(d): Probability distributions of w_{cld} as a function of height. The mean is shown by the red line, the time-mean of the minimum and maximum are shown in yellow, and the time-mean 10th and 90th percentiles are shown in orange lines. Panel (e) shows the 50th, 90th, and 99th percentiles of each time step of hiSLAM’s probability distribution of w_{cld} . SLAM = Spherical Limited Area Model.

and magnitudes. For this reason we find that hiSLAM is deep-convection-permitting, meaning that it, in a statistical sense, represents deep convection realistically.

3.2.2. Temperature Anomalies

The probability distributions of T'_{cld} as a function of height are shown in Figure 7. In our models clouds below the freezing level (~ 6 km) are mostly colder than their environment, and only warmer above the freezing level. The cool anomalies relate to downdrafts, shallow, and congestus cloud tops, while the warm anomalies represent buoyant updrafts.

The parameterization of convection used in coSLAM-pc does, in terms of the mean vertical profile, represent T'_{cld} in clouds similarly to simulations with explicit convection. However, the spread of T'_{cld} is, compared

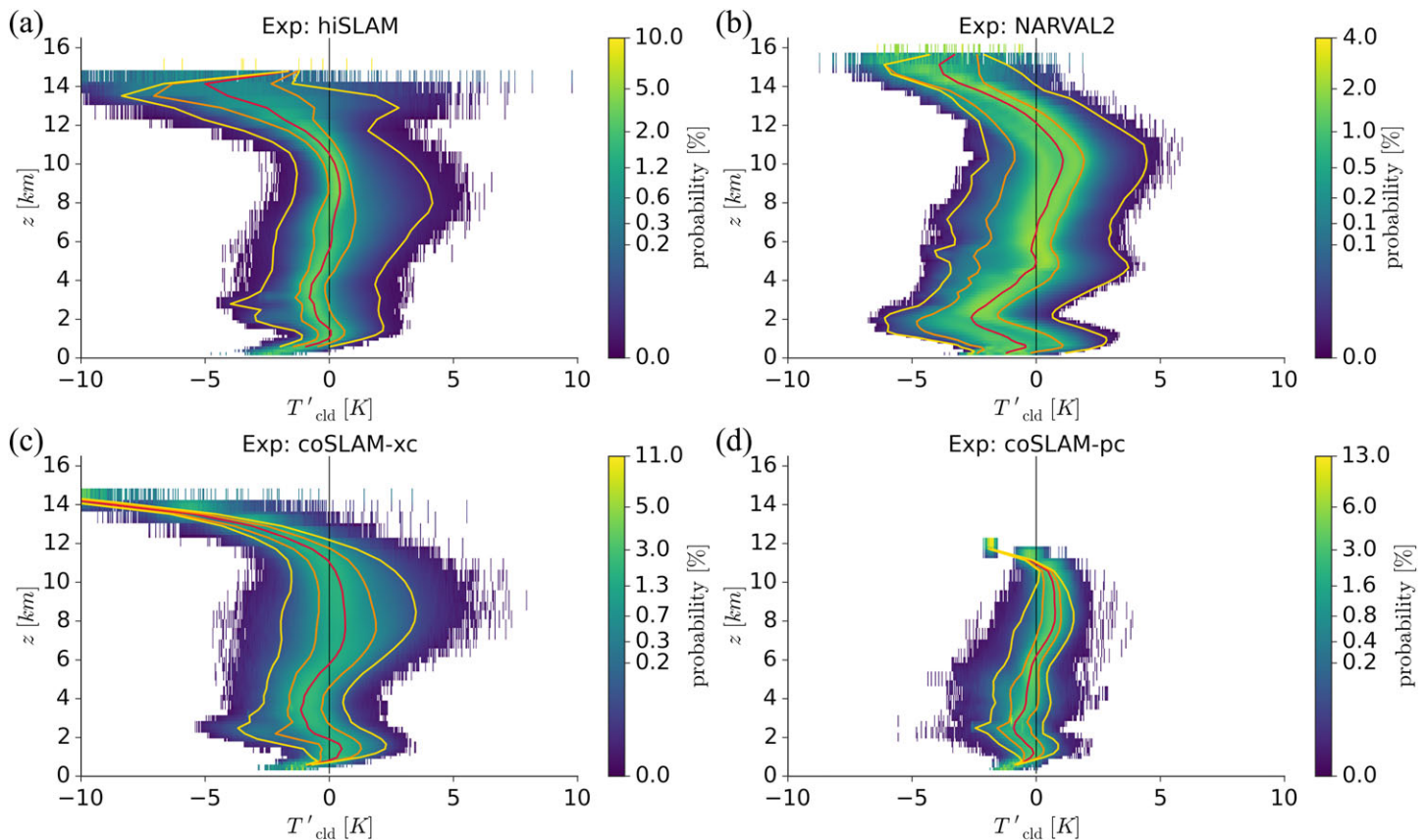


Figure 7. Panels (a)–(d): Probability distributions of T'_{cld} as a function of height. The mean is shown by the red line, the time-mean of the minimum and maximum are shown in yellow, and the time-mean 10th and 90th percentiles are shown in orange lines. SLAM = Spherical Limited Area Model.

to coSLAM-xc, slimmer, meaning a reduced variability of in-cloud temperature anomalies. Thus, a parameterization of convection affects the dynamical representation of convection much more strongly than the thermodynamical representation.

In comparison to hiSLAM, NARVAL2 shows cooler T'_{cld} at low levels. This indicates drier low-level and midlevel environmental conditions and inversion layers, causing more evaporation and cooler downdrafts, along with a greater variety of lifting mechanisms. At ~ 5.5 km, where cloud fraction shows a local maximum (see Figure 5a), the mean of T'_{cld} turns positive and there is a localized increase in variability, both in the positive and negative. The mean of T'_{cld} stays positive up to ~ 12 km. Above that overshooting tops and radiative cooling cause clouds being cooler than their environment again.

Both hiSLAM and NARVAL2 differ from coSLAMs in that T'_{cld} does not converge toward the cloud tops. Instead, the spread of the distribution of T'_{cld} widens there. We interpret this signal, like for w_{cld} , as gravity waves and oscillations around the level of neutral buoyancy.

3.2.3. Latent Heat

Latent heating in clouds is used in current gravity wave parameterizations as a measure of convective activity in order to compute gravity wave drag (Richter et al., 2010). Cloud microphysical parameterization estimate the heat release of the relevant processes, condensation, evaporation, and freezing. A parameterization of convection, as used in coSLAM-pc, introduces a heating tendency that adds to the latent heating.

The probability distributions of latent heating rates Q_{lat} are presented in Figure 8. For hiSLAM and coSLAM-xc the mean of Q_{lat} peaks at ~ 6 km, which is approximately the freezing level. Also for coSLAM-pc a local maximum appears there. At higher levels the models behave similarly. Only in hiSLAM we find cooling above ~ 6 km, which can be explained by the melting of cloud ice. In coSLAM-xc there are two spikes at ~ 1 and ~ 3.5 km. Those are expected to be caused by the under-resolved character of convection in the model, owing to the abrupt release of large latent heat of condensation once the grid cell is saturated. For all models the distribu-

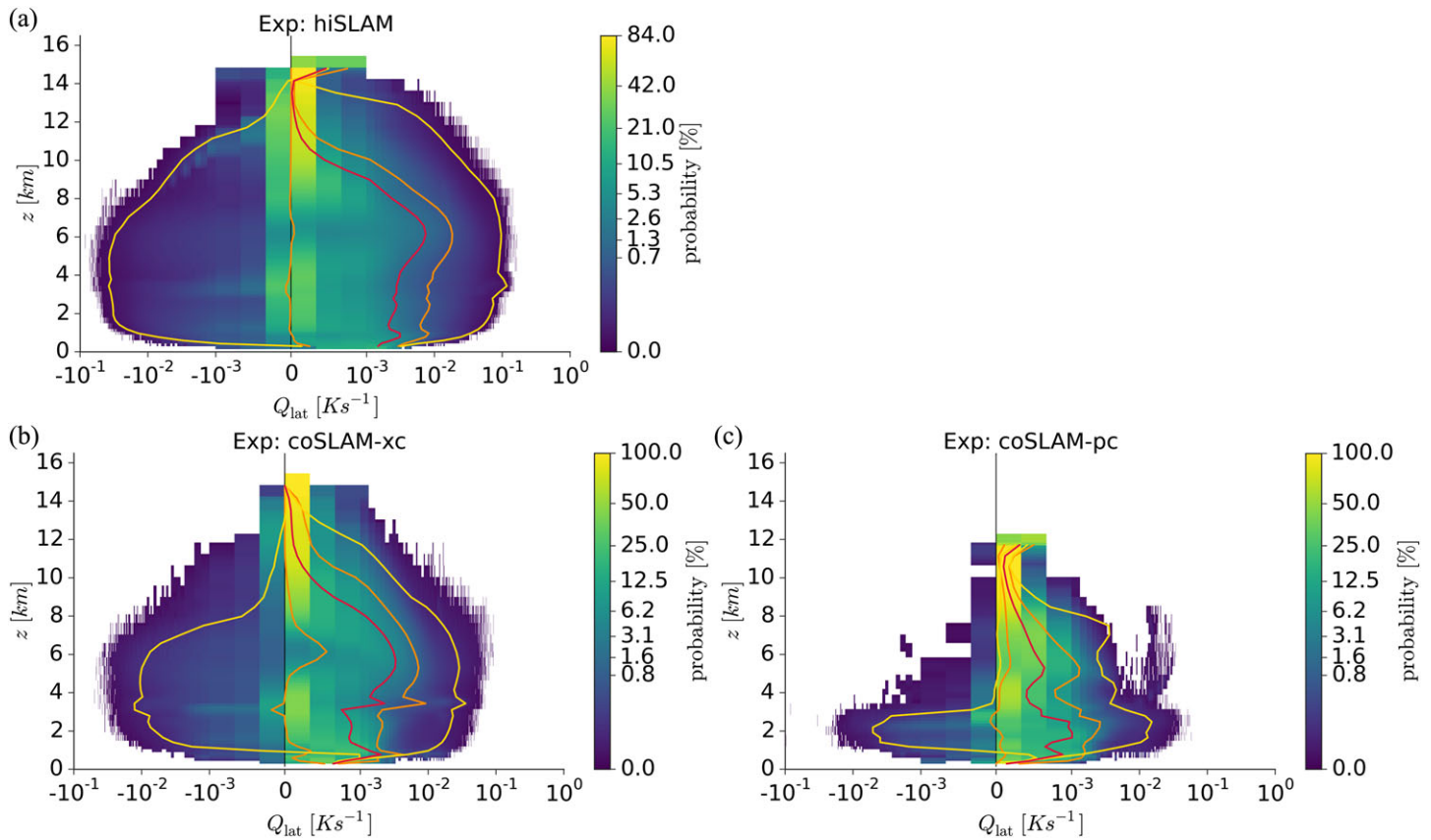


Figure 8. Panels (a)–(c): Probability distributions of Q_{lat} as a function of height. The mean is shown by the red line, the time-mean of the minimum and maximum are shown in yellow, and the time-mean 10th and 90th percentiles are shown in orange. Note that the x axis is only linear within ± 0.001 K/s and logarithmic everywhere else. Note that the latent heating rate was only available for SLAMs, and not for NARVAL2. SLAM = Spherical Limited Area Model.

tion converges toward the cloud tops. This is in line with our interpretation of the temperature perturbations at cloud tops seen in hiSLAM (Figure 7a). They do not appear to be a result of latent heating, but rather of an vertical oscillation of overshooting tops or gravity waves.

In coSLAM-pc the spread of the probability distribution and the magnitude of Q_{lat} , in terms of its mean and its time-mean maximum, is less than in the models with explicit convection, in particular for altitudes greater than 3 km.

We see from the vertical profiles of the time mean and of the time means of the 90th percentile and maximum that the latent heating is stronger in hiSLAM than in coSLAM-xc. Thus, the latent heating, as expected, correlates with the updraft velocities shown in Figure 6, where we also find that hiSLAM is more intense than coSLAM-xc.

We will further examine the spatial variability of latent heating through a spectral analysis of its proxy precipitation (see subsection 3.3).

3.3. Spectral Analysis of Precipitation Flux, Vertical Velocity, and Kinetic Energy at 9.5 km

In the tropics precipitation is a natural proxy for deep convective clouds, as these precipitate and produce the most of it. Thus, precipitation fits well for discriminating between deep convection, the main source of CGGWs, and nonprecipitating shallow convection. Furthermore, precipitation is proportional to the net heating of a cloud, and thus also estimates the thermal forcing of gravity waves.

In Figure 9a the zonal wave number spectra of precipitation flux defined as the mass of precipitation per unit area and time is shown. hiSLAM and coSLAM-xc are similar, for scales commonly resolved. Compared to them, coSLAM-pc misses a lot of variance for common scales and shows a steeper spectral slope. ICSOM1 and NARVAL2 exhibit larger precipitation flux variance than SLAMs, which is consistent with their greater magnitudes of vertically integrated water vapor and cloud water. Only hiSLAM contains more variance for

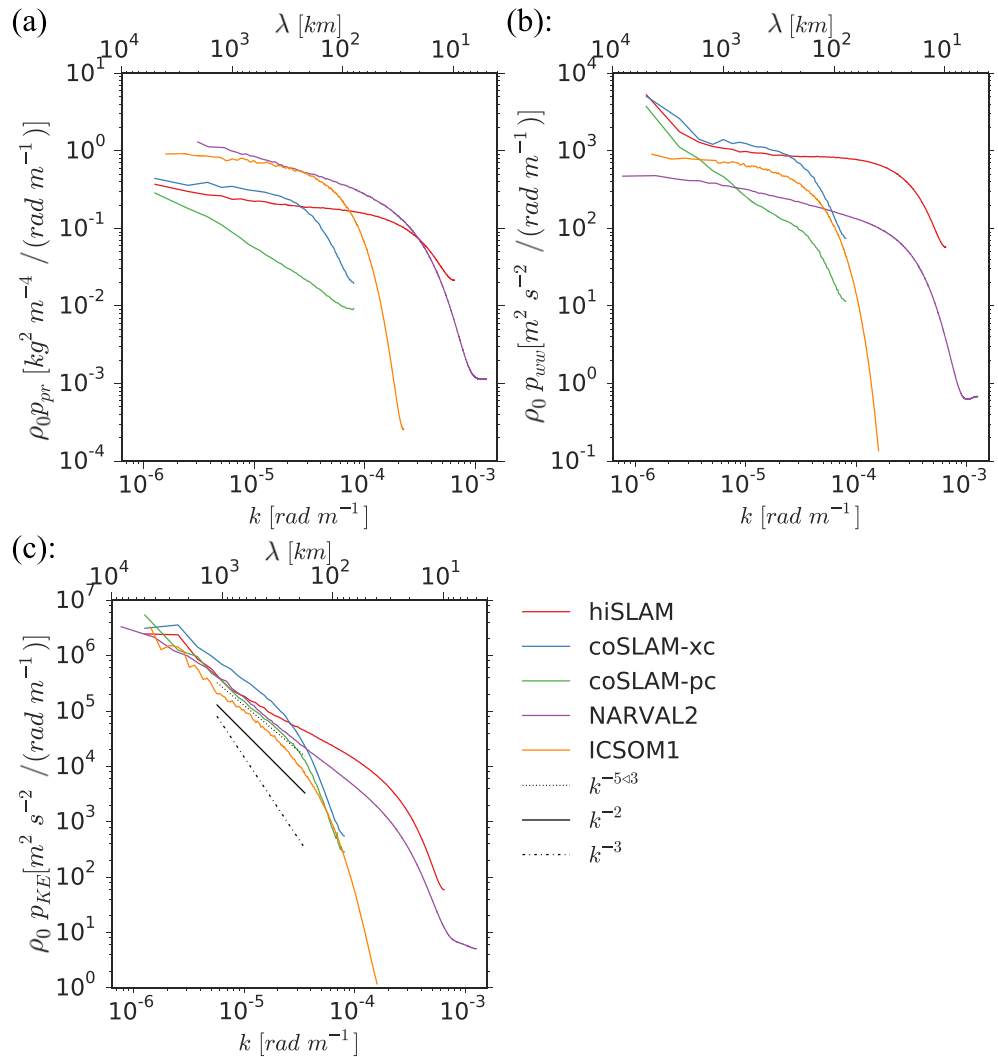


Figure 9. Power spectral densities of (a) precipitation flux variance (b) of vertical velocity variance, wv , at ~ 9.5 km height and (c) of kinetic energy, KE , also at 9.5 km height, in zonal wave number space. SLAM = Spherical Limited Area Model; ICSOM = Interhemispheric Coupling Study by Observations and Modeling.

scales smaller than 20 km. For all models but coSLAM-pc, the zonal wave number spectrum of precipitation flux is flat until scales at which numerical diffusion sets in.

Figure 9b shows the zonal wave number spectrum of vertical velocity at 9.5 km. Through the buoyancy force, the latent heating and vertical motion in the tropical troposphere are intrinsically coupled. For this reason the similarities in their spectra are not surprising. Unlike the spectrum of precipitation, the vertical velocity variance of hiSLAM here exceeds that of NARVAL2. This is another indication for the high intensity of updraft velocities in hiSLAM and for the efficient translation of heating into vertical motion in the absence of a background flow.

We will refer back to these spectral properties, that characterize the forcing of gravity waves, to explain differences among the simulations' spectra of gravity wave momentum flux in the stratosphere (see subsection 4.1).

For upper tropospheric kinetic energy a spectral slope proportional to $k^{-5/3}$ was proposed for tropical dynamics (going back to Kraichnan, 1967), where the flow is mostly divergent, and has been confirmed in observations (Nastrom et al., 1984) and numerical model studies (e.g., Koshyk & Hamilton, 2001). Figure 9c shows the power spectral density of kinetic energy in zonal wave number space at altitudes of ~ 9.5 km. The characteristic spectral slope is reproduced by all models except hiSLAM, for the scales unaffected by

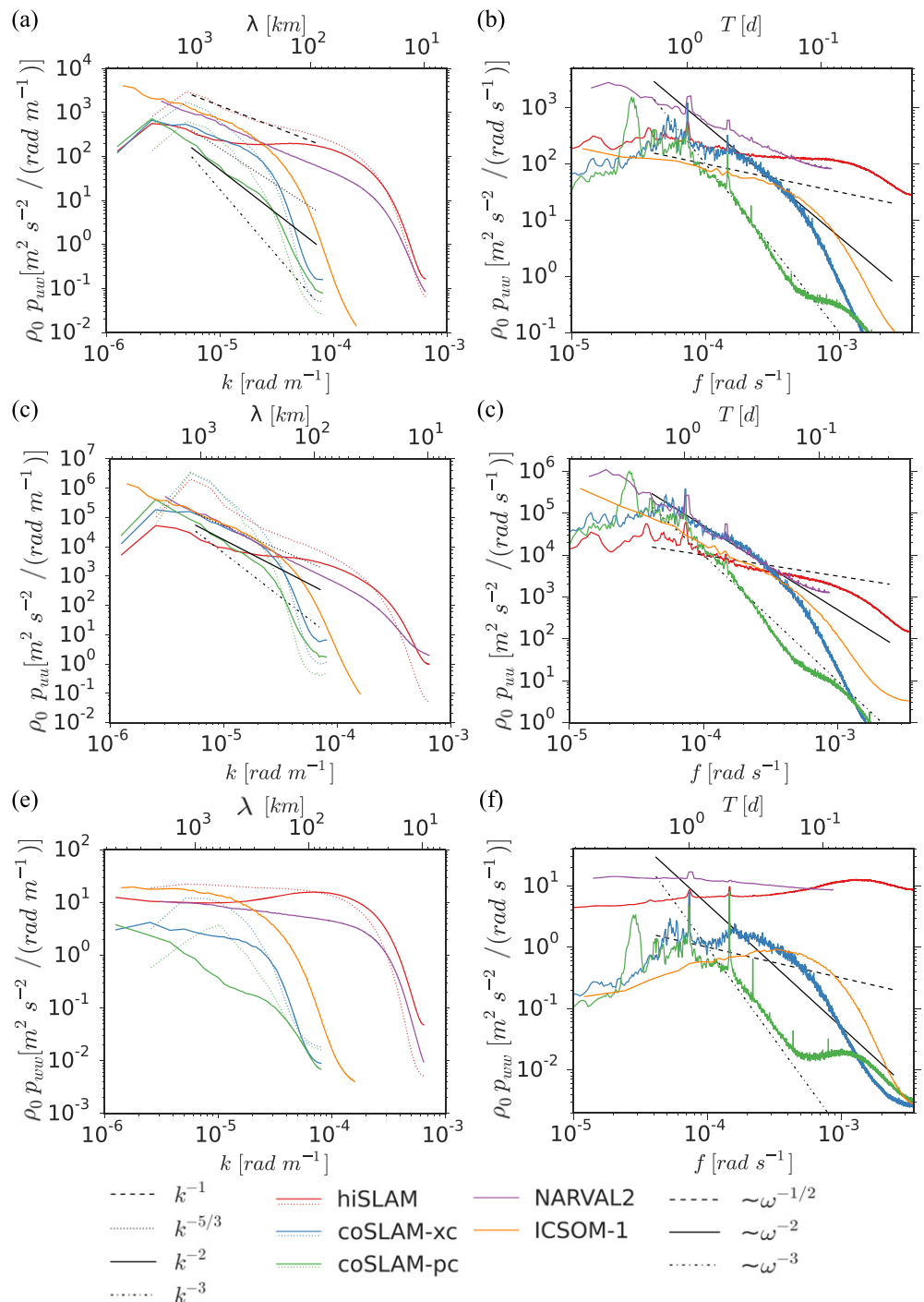


Figure 10. Power spectral densities of (a and b) zonal momentum flux, uw , (c and d) zonal velocity variance, uu , and (e and f) vertical velocity variance, ww at ~ 20 km height. Panels on the left side show the spectra in zonal wave number space and panels on the right side in frequency space. Dotted lines of SLAM simulations show their meridional momentum flux variance (a), the meridional (c), and vertical (e) velocity variance in meridional wave number space, computed over the entire domain. SLAM = Spherical Limited Area Model; ICSOM = Interhemispheric Coupling Study by Observations and Modeling.

Table 3

Intercomparison of the Absolute Momentum Flux, Which is Given by the Integration Over the Zonal Wave Number Space of p_{uw}

	hiSLAM	coSLAM-xc	coSLAM-pc	NARVAL2	ICSOM1
hiSLAM /	1	0.10	0.02	0.95	1.28

Note. In order to neglect the influence of the large scales, we only integrate over wavelengths shorter than 1,000 km. The absolute momentum flux of all simulations is divided by that of hiSLAM. SLAM = Spherical Limited Area Model; ICSOM = Interhemispheric Coupling Study by Observations and Modeling.

numerical diffusion. We find that hiSLAM's spectrum is flatter than $k^{-5/3}$ and thus contains an excess of kinetic energy at small scales. Quantitatively ICSOM1 resolves the least kinetic energy of all experiments, and coSLAM-pc resolves the least energy among all SLAMs. hiSLAM resolves most kinetic energy at scales less than ~ 250 km and exceeds NARVAL2, with equal grid spacing, significantly, due to its flatter slope.

4. Spectral Analysis of CGGWs

We characterize gravity waves excited by convection, as described in section 2.3, by spectral analyses of gravity wave properties in the stratosphere. It is assumed that perturbations in the stratosphere relate to gravity waves that were excited by convective clouds in the troposphere.

4.1. Spectra in Zonal Wave number and Frequency Space

Here we analyze spectra in both zonal wave number and frequency space, shown in Figure 10, of zonal momentum flux uw , zonal velocity u , and vertical velocity w in the stratosphere, that are characteristic properties of gravity waves.

Figure 10a shows the power spectral density of zonal momentum flux variance in zonal wave number space. At scales greater than 200 km simulations with background rotation, ICSOM1 and NARVAL2, contain more variance than SLAM models. This signal relates to equatorial waves relying on the beta effect, like Kelvin, Rossby-Gravity, and inertia-gravity waves, or to baroclinic waves from midlatitudes. For scales smaller than ~ 250 km, however, hiSLAM exceeds NARVAL2 in zonal momentum flux variance. The zonal momentum flux spectrum of hiSLAM flattens and becomes *white*. This behavior is consistent with the results presented by Lane and Moncrieff (2008), who also find a white spectrum until scales at which numerical diffusion sets in. In contrast to that, for the realistic simulations, NARVAL2 and ICSOM1, and for coSLAM-xc, the zonal momentum flux spectrum has a steady slope $\sim k^{-1}$. Still a substantial amount of momentum is contained at small scales and missed by models with coarse resolution.

coSLAM-pc resolves the least zonal momentum flux of all models, also in comparison to the equivalent simulation without a parameterization of convection, coSLAM-xc. This means that a parameterization of convection affects gravity wave generation through convection and causes a reduction of momentum flux carried by CGGWs into the middle atmosphere. Zonal momentum flux controls wave mean-flow interaction in the middle atmosphere, and thus middle atmospheric circulations are expected to be affected by the use of a parameterization of convection, unless effects of parameterized convection on momentum flux are parameterized as well. A comparison to the zonal wave number spectra of precipitation flux, representative of net diabatic heating, and upper-tropospheric vertical velocity variance (see Figure 9) shows consistent correlations. It indicates that coSLAM-pc's lack in diabatic heating variance at small scales, causes not only reduced vertical velocity variance in the upper troposphere, but manifest also in the reduction of zonal momentum flux variance of gravity waves in the stratosphere.

The integration of the zonal momentum flux over zonal wave number space quantifies the potential forcing of the wave field onto the mean circulation. We thus in Table 3 compare this quantity with respect to hiSLAM, for scales shorter than 1,000 km. Among SLAMs we find that hiSLAM contain 10 times more absolute momentum flux than coSLAM-xc. The reduction of absolute momentum flux by a parameterization is found to be a factor of 5 when comparing coSLAM-pc to coSLAM-xc. NARVAL2 and ICSOM1 exceed hiSLAM in momentum flux at scales greater than 250 km and fall below hiSLAM at shorter scales. Thus, in this analysis NARVAL2 shows slightly less and ICSOM1 more absolute momentum flux than hiSLAM.

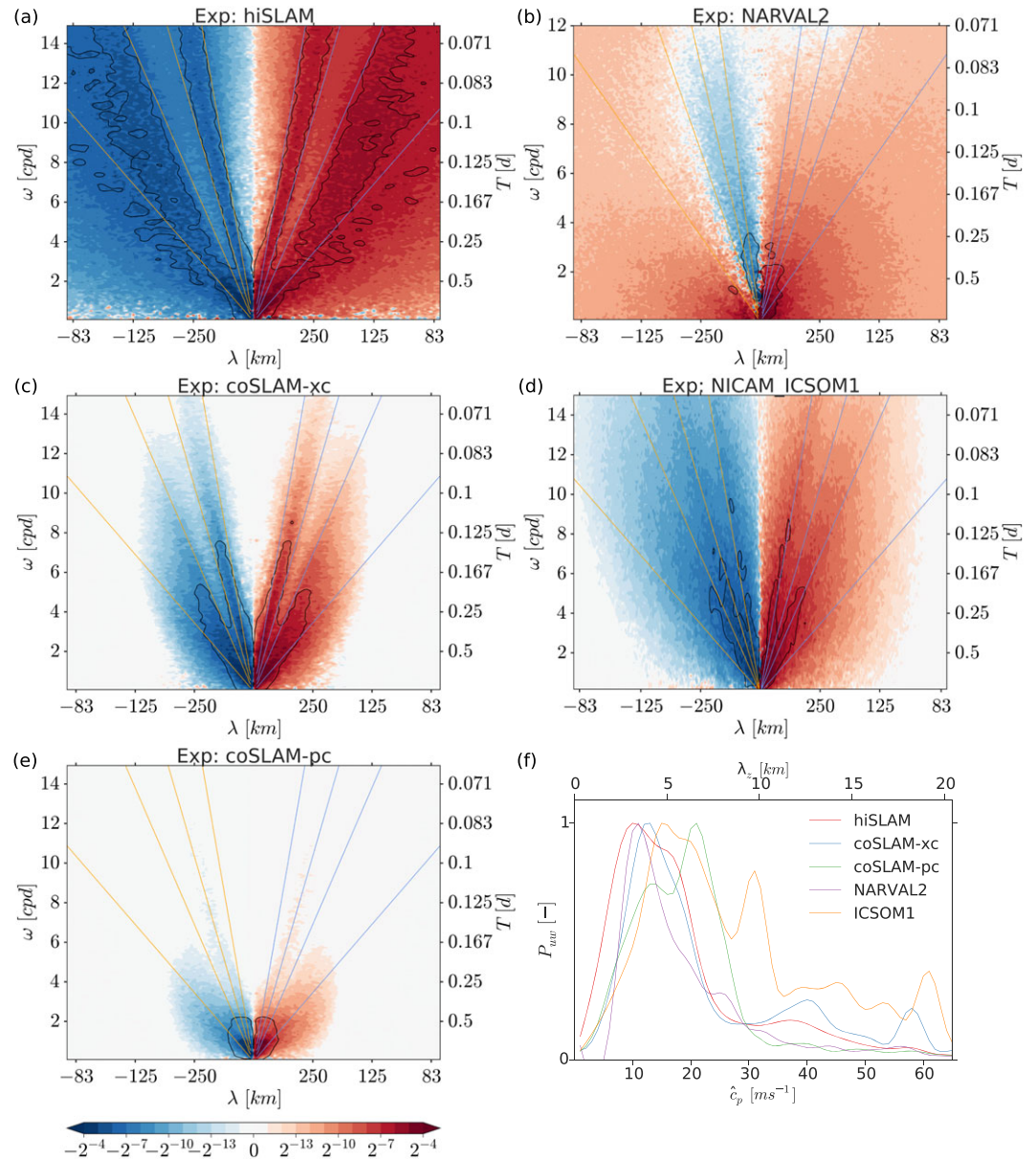


Figure 11. Panels (a)–(e): Cross-spectral power of zonal momentum flux, P_{uw} [–], normalized by its maximum value, in zonal wave number–frequency space at ~ 20 km height. Black contours in panels (a)–(e) indicate variance higher than that of a smoothed background and thus highlight gravity wave modes. Blue and orange lines display the linear gravity wave dispersion relation (see Equation (4)) of constant horizontal phase speeds. The flattest line refers to a magnitude of 10 m/s, and the steeper lines to 20, 30, and 50 m/s. Panel (f): P_{uw} [–] as a function of intrinsic zonal phase speed, \hat{c}_p , and vertical wavelength, λ_z . SLAM = Spherical Limited Area Model; ICSOM = Interhemispheric Coupling Study by Observations and Modeling.

The frequency spectra of gravity wave momentum flux of SLAMs, shown in Figure 10b, are consistent with the zonal wave number spectra. The power spectral densities of coSLAM-pc are significantly weakened by its parameterization of convection. coSLAM-xc and hiSLAM show similar results down to periods of half a day. hiSLAM’s spectrum is generally flat and dissipation sets in at scales shorter than an hour. The spectra of the realistic simulations, ICSOM1 and in particular NARVAL2, however do show persistent slopes that are flatter than ω^{-1} .

In the upper troposphere the slope of zonal wave number spectra of horizontal velocity is proportional to $k^{-5/3}$, as shown with aircraft observations in Gage and Nastrom (1986a, 1986b). For the stratosphere, Gardner et al. (1993) showed, by using an analytical gravity wave model, that a wave number spectrum of zonal veloc-

ity is also proportional to $k^{-5/3}$ —a universal property of the gravity wave spectrum. The zonal wave number spectra of zonal velocity at 20 km are shown in Figure 10c. The realistic simulations, NARVAL2 and ICSOM1, as well as coSLAM-xc confirm the proposed spectral slope at all scales unaffected by numerical diffusion. For coSLAM-pc the spectrum has, as for the other spectra before, a steeper slope than $k^{-5/3}$ and is therefore unsaturated. This confirms that the forcing of CGGWs is weakened by a parameterization of convection. For hiSLAM the spectrum has the least variance at large scales and is almost flat for scales smaller than 500 km. Lane and Moncrieff (2008) also obtained an almost flat spectrum for zonal velocity variance in zonal wave number space. We propose that the enhancement of small scales, as also seen in zonal momentum flux, is due to performing the spectral analysis locally above the intense and persistently organized convective system only. By that the *potential* of convection in its generation of gravity waves is revealed.

For the power spectral density of kinetic energy and zonal velocity in frequency (ω) space, associated with gravity waves, a spectral slope proportional to ω^{-2} was postulated, based upon analytical gravity wave models (Gage & Nastrom, 1985; Gardner et al., 1993). This applies for the frequency range from buoyancy frequency N to planetary rotation f . The power spectral density of zonal velocity in frequency space is shown in Figure 10d. The proposed spectral slope of ω^{-2} is reproduced well by the realistic simulations, ICSOM1 and in particular by NARVAL2. But also, for a limited part of the frequency space, the spectrum of coSLAM-xc follows this spectral slope. The spectra of hiSLAM and coSLAM-pc have again too flat and too steep slopes, respectively.

Figure 10e shows the zonal wave number spectra of vertical velocity variance at 20 km. The spectra are generally flat, NARVAL2 showing an almost purely white wave number spectrum. hiSLAM even develops a peak at ~ 100 km, which was also found in Lane and Moncrieff (2008). The spectrum of coSLAM-pc however has a steep slope, meaning that variance decreases toward smaller scales for the scales well resolved. We interpret this as another manifestation of the lack of small scale variance in latent heating through convection.

The frequency spectrum of vertical velocity variance is shown in Figure 10f. The diurnal cycle and its modes can be identified clearly, in particular for coSLAM-pc. The high resolution experiments, NARVAL2 and hiSLAM, have the greatest variance here and have flat spectral slopes for the whole frequency range. However, while the variance decreases slightly toward higher frequencies for NARVAL2, it increases and develops a peak for SLAM. The coarser models show peaks in their spectra within the range of a 0.5 and 10 cpd, and are affected by numerical diffusion toward higher frequencies.

For all spectra the spatial resolution impacts not only spectra in wave number space but also in frequency space. This means a reduction of variance at smaller temporal scales goes along with coarsening spatial resolution and with applying a parameterization of convection.

Dotted lines in Figure 10 show SLAMs' spectra in meridional wave number space, that are computed over the entire domain and for this reason attributed as global. In panel Figure 10a the meridional momentum flux, in Figure 10c the meridional, and in Figure 10e the vertical velocity variance are shown. We generally find that larger scales are enhanced, suggesting that larger scale waves only evolve in a distance from convection. For this reason hiSLAM's spectral slope of momentum flux variance converges toward k^{-1} for scales greater 250 km and still flattens toward smaller scales. Also, its spectrum of meridional velocity variance becomes proportional to $k^{-5/3}$. For the global vertical velocity variance the peak at small scales vanishes, the spectrum flattens and becomes similar to that of NARVAL2. In regards of coSLAMs large scales are enhanced also and spectral slopes steepen.

4.2. Zonal Wave Number-Frequency Spectra

Figure 11 shows zonal momentum flux variance in wave number-frequency space at a height of ~ 20 km, with a decomposition of eastward- and westward-propagating waves, following Hayashi (1971).

hiSLAM's spectrum shows a broad and smooth lobe of slower zonal phase speeds and a sharper lobe of faster phase speeds, which both represent prevailing gravity wave modes. This shape is again consistent with the equivalent spectrum presented in Figure 8 of Lane and Moncrieff (2008). coSLAMs, limited through their coarser resolution at shorter wavelengths, are also limited in their variance at higher frequencies. This is particularly true for coSLAM-pc, a result which was found in section 4.1 already. Nevertheless, for both coSLAM-xc and coSLAM-pc, two prevalent gravity wave modes can be anticipated from the spectra's two-lobe structure.

For all SLAM simulations the zonal wave number-frequency spectra are symmetric around the zonal mean, as expected due to the absence of a zonal circulation and vertical shear. Thus, their net wave forcing on the background zonal flow is zero.

The structure of two lobes is also reproduced in ICSOM1, and the spectrum is quite symmetric with respect to eastward and westward propagating waves, similar to those of the idealized SLAM simulations. This is because the mean background zonal wind, \bar{u} , is weak at this altitude (~ 1.5 m/s).

The spectrum of NARVAL2 however shows strong asymmetry. This indicates a zonal background flow, which is on average ~ -18 m/s, and which interacts with and filters the propagating waves. Only fast waves, with zonal phase speeds greater than the background flow, propagate westward. The mean background flow can be seen in Figure 2b and layers with strong vertical shear can be identified in the lower stratosphere. The two lobes seen in all other models' spectra can not be identified.

Figure 11f shows the variance of zonal momentum flux as a function of intrinsic zonal phase speed, \hat{c}_p , and vertical wavelength, λ_z , following Beres et al. (2002). Although our models are based on nonhydrostatic primitive equation, here we use the gravity wave dispersion relation in Boussinesq-Approximation, given as

$$\hat{\omega}^2 = \frac{N^2 k^2}{k^2 + m^2} \quad (4)$$

with a Brunt-Väisälä frequency N of 0.02 s^{-1} and k and m the horizontal and vertical wave numbers. Assuming that $m \gg k$, equation (4) simplifies to

$$\hat{\omega} = \frac{Nk}{m}, \quad (5)$$

and c_p becomes directly proportional to λ_z and can be expressed as

$$\hat{c}_p = \frac{\hat{\omega}}{k} = \frac{N\lambda_z}{2\pi}. \quad (6)$$

The assumption of a Boussinesq, hydrostatic case plays a role for high-frequency gravity waves where $\omega \ll N$ and short scale gravity waves for which $m \gg k$ is not satisfied. The first relation holds as the highest resolved frequency scales with the model output frequency of 15 min. The assumption $m \gg k$ weakens the accuracy of the analysis for gravity waves of short horizontal scales. Despite compromising on accuracy we still present this analysis as it allows to identify vertical gravity wave modes. The credibility of deep modes may appear weak, as their scale approaches the distance from the tropopause up to the model top. However, we assume that there is no wave-reflection at the model top and that gravity waves are upward propagating. Further, the vertical scale of gravity waves is deduced indirectly from the zonal wave number and frequency. With these assumption considered we expect the limited vertical domain size of the models to not play a role here.

As a result $P_{uw}(\hat{c}_p, \lambda_z)$, shown in Figure 11f, exposes distinct gravity wave modes, that could also be inferred from the lobes of wave number-frequency spectra. All simulations show two or more vertical modes, one shallow mode with vertical scales between 3 and 6 km, and larger modes with vertical wavelengths of up to 20 km.

Salby and Garcia (1987) showed, that through the projection response, the dominant vertical wavelength is expected to be equal to twice the vertical scale of latent heating. Figure 5b shows the distribution of the depth of latent heating. It is computed for each column as the sum of heights of cells where $Q_{\text{lat}} > 1 \times 10^{-5} \text{ K s}^{-1}$. It can be seen that heating depths are mostly shallow, like the profile of cloud fraction suggests (see Figure 5a). However, although coSLAM-pc has a great fraction of high clouds, its heating depths are limited in their vertical scale and very rarely exceed 6 km. hiSLAM and coSLAM-xc have a significant fraction of columns with deep heating (> 8 km). In particular, coSLAM-xc shows a peak of heating depths with a scale of ~ 9 km. These two characteristics, coSLAM-pc's lack of deep heating and coSLAM-xc's peak in deep heating, project onto their prevalent vertical gravity wave modes, shown in Figure 11f. For coSLAM-pc a vertical mode with a peak at ~ 7 km is dominant, and no deeper modes exist. This corresponds well to the distribution of heating depths, with the peak at ~ 3 km being, as proposed by Salby and Garcia (1987), half of the vertical scale of the prevalent gravity wave mode, with a scale of ~ 6 km. The same relation holds for the deep mode of heating in coSLAM-xc. Its scale of ~ 9 km projects exactly onto a deep gravity wave mode, that can be identified as a peak at ~ 18 km. The distribution of heating depths of hiSLAM is more homogeneous, and thus the response in deep vertical gravity wave modes is not as pronounced as in coSLAM-xc. hiSLAM shows a particularly broad shallow mode, with a peak at a vertical wavelength of ~ 3 km.

For ICSOM1 we identify three dominant modes, one shallow mode at ~ 5 , a medium mode at ~ 10 , and a deep mode at ~ 19 km. Unfortunately, we can not put these into relationship with heating rates.

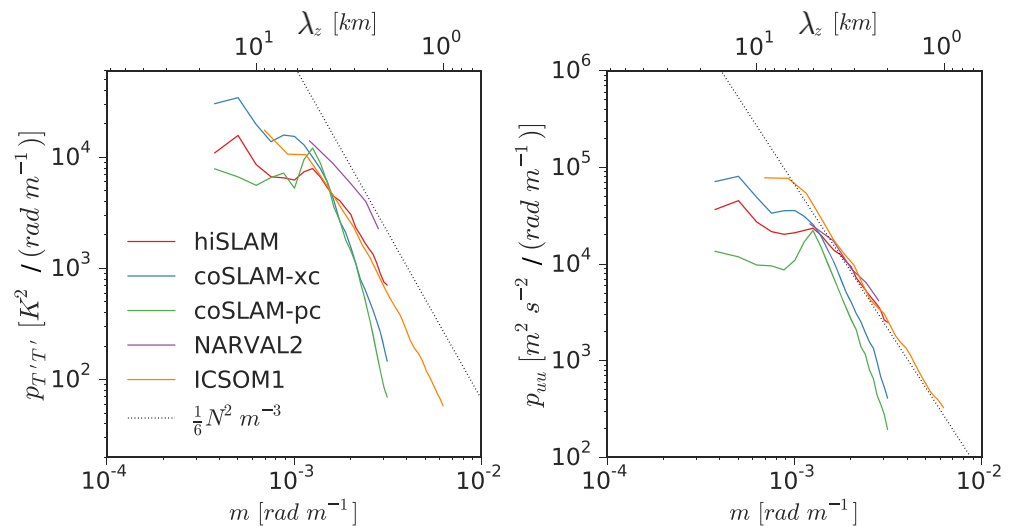


Figure 12. Power spectral densities of (a) zonal velocity variance, uu , and (b) temperature anomaly variance, $T'T'$, in vertical wave number space. SLAM = Spherical Limited Area Model; ICSOM = Interhemispheric Coupling Study by Observations and Modeling.

NARVAL2 only has a shallow dominant gravity wave mode with a scale of ~ 4 km. This seems to be consistent with the vertical profile of cloud fraction that shows a great amount of shallow convection and thus suggest mostly shallow latent heating.

Although the projection response of Salby and Garcia (1987) can be identified in SLAMs, it has to be considered, that Holton et al. (2002) showed, that the relation of diabatic heating and the vertical scale of the gravity wave response is dependent upon all spatial and temporal scales of the heating. We will look further into this matter by vertical wave number spectra, presented in the following section 4.3.

4.3. Vertical Wave Number Spectra

Here we investigate the vertical wave number (m) spectra of gravity wave properties zonal velocity u , temperature anomaly T' , and vertical velocity w . For horizontal velocity and temperature anomaly a spectrum proportional to m^{-3} was observed (by Tsuda et al., 1989; and recently Zhang, Huang, Huang, Gong, et al., 2017; Zhang, Huang, Huang, Zhang, et al., 2017; Zhao et al., 2017). This was explained by the saturation of gravity waves and was confirmed in simple gravity wave models that, within the scales of the saturated regime, yielded a spectrum equal to $\frac{N^2}{6m^3}$ (Dewan & Good, 1986; Smith et al., 1987; Weinstock, 1985b), with N being the buoyancy frequency. The dominant vertical mode can be identified as the wave number of the peak of the spectrum, separating the unsaturated from the saturated part of the spectrum. For scales smaller than the buoyancy wave number, the spectrum is governed by turbulence and follows a spectral slope of $m^{-5/3}$. In numerical models the vertical resolution was found to play a role in the representation of gravity waves in the middle atmosphere (Watanabe et al., 2015). For this reason the models' vertical grids, shown in Figure 1, have to be considered. In Figure 12 the vertical wave number spectra of zonal velocity u (Figure 12a) and temperature anomaly T' (Figure 12b) are shown.

For hiSLAM the expected spectrum of $p_{uu}(m) = \frac{N^2}{6m^3}$ is reproduced in the wavelength range from 2 to 5 km. coSLAMs both do not reproduce this, with too steep slopes and too little variance at short vertical scales. The same holds for the spectrum of $p_{T'T'}(m)$, with only hiSLAM reproducing a spectral slope proportional to m^{-3} . Dominant vertical gravity wave modes are expected to show up as peaks of the spectra. For hiSLAM and coSLAM-xc we here find in both spectra the dominant wavelengths at ~ 15 km, which is the mode excited by deep convection. For coSLAM-pc the spectra have peaks at a wavelength of ~ 5 km. Both are consistent with the dominant modes deduced from zonal wave number-frequency spectra in section 4.2: coSLAM-xc has a deep mode, that is more pronounced than that of hiSLAM, and coSLAM-pc fails to generate a deep mode. Furthermore, coSLAMs differ little in their variance at short scales. coSLAM-pc's lack in gravity wave variance, as shown in section 4.1, is found in the lack of a deep gravity wave mode, and ultimately in the lack of a deep mode of latent heating. SLAM's vertical grid contains 26 levels in between 15 and 55 km, with a grid spacing

Table 4

Evaluation of Universal Spectral Slopes: "v" Means That the Model Yields the Spectral Slope Proposed by Prevalent Theories

	$p_{KE}(k) \sim k^{-5/3}$	$p_{uu}(k) \sim k^{-5/3}$	$p_{uu}(m) \sim m^{-3}$	$p_{T'T'}(m) \sim m^{-3}$	$p_{uu}(\omega) \sim \omega^{-2}$
hiSLAM	x-flat	x-flat	v-[2;5]	v-[2;5]	x-flat
coSLAM-xc	v	v	x-steep	x-steep	v
coSLAM-pc	v	x-steep	x-steep	x-steep	x-steep
ICSOM1	v	v	v-[1;8]	v-[1;5]	v
NARVAL2	v	v	v	v	v

Note. In brackets the scales of wavelengths, in units of km, are given, for which the proposed spectrum is reproduced by our models. x-steep and x-flat stand for spectral slopes steeper or flatter than the proposed spectral slope. SLAM = Spherical Limited Area Model; ICSOM = Interhemispheric Coupling Study by Observations and Modeling.

ranging from 670 to 1,100 m. It is the model with the highest model top and allows to robustly analyze gravity waves with scales up to ~ 15 km by means of a spectral analysis in the vertical dimension.

ICSOM1 reproduces the spectrum $p_{uu}(m) = \frac{N^2}{6m^3}$ for vertical wavelengths from 1 to 8 km. Also for temperature anomaly variance the spectral slope is proportional to m^{-3} from 1 to 6 km. It is important to note, that ICSOM1's vertical grid has a constant spacing of 200 m between 15 and 20 km and contains 38 levels between 15 and 38 km. As such it is the model with the highest vertical resolution, allowing gravity waves with vertical scales down to ~ 1 km to be resolved explicitly.

For NARVAL2 the expected spectrum of $p_{uu}(m) = \frac{N^2}{6m^3}$ is reproduced for vertical scales shorter than ~ 8 km. The grid spacing ranges from 500 to 1,100 m for altitudes greater than 15 km, with a model top at 30 km. As for ICSOM1, we can not identify the dominant modes deduced from zonal wave number-frequency Spectra (see Figure 11f), due to the limited vertical extent of the model domain.

Note that the main assumption going into this analysis of vertical wave number spectra is that the Brunt-Väisälä frequency is constant throughout the vertical space investigated. By that the vertical wavelength of a gravity wave would remain unaffected during its upward propagation. Also, the effects of changing vertical grid spacing and damping layers below the model top are neglected. Still we find that the results, as indicated by the reproduction of the universal gravity wave spectrum, are robust for a limited vertical range.

5. Discussion

5.1. On Modeling the Universal Gravity Wave Spectrum

Universal properties of middle atmospheric gravity waves show in one-dimensional spectral space and are summarized in Gardner et al. (1993). The saturation of the gravity wave spectrum means that, within the scales of the dominant wave number and buoyancy wave number, the power spectral density of gravity wave properties is limited by convective and shear instability criteria. In simple analytical gravity wave models, based upon only their dispersion and polarization relations, the spectral slopes were found to be proportional to power-law relations.

In Table 4 the results of spectral analyses of our models, with respect to the reproduction of proposed spectral slopes, are summarized.

We find that the models with realistic boundary conditions, ICSOM1 and NARVAL2, yield the proposed spectral slopes in all one-dimensional spectra of gravity wave properties.

hiSLAM succeeds in producing the proposed spectra in vertical wave number space, where both coSLAMs appear too steep. For hiSLAM the spectral slopes, of both zonal-wave number and frequency spectra, are flat. We find that this result is due to applying the gravity wave analysis above the convective cluster, within $\pm 10^\circ$ latitude. It is a local and near-field gravity wave spectrum and thus reveals the potential of convection to generate gravity waves.

coSLAM-xc produces the proposed spectral slopes in zonal wave number and frequency space, for spectral scales resolved. For coSLAM-xc and coSLAM-pc the slopes in vertical wave number spectra are too steep, suggesting that gravity waves of short vertical scale do not reach saturation. Further, coSLAM-pc's spectra are generally too steep, meaning that gravity waves are weakened at short spatial and temporal scales by a parameterization of convection.

We may also note that a basic property of the analytical gravity wave model of Gardner et al. (1993) is that the spectral slopes in horizontal wave number space and in frequency space are proportional. This aspect we find realized in the consistently steep and flat slopes of SLAMs in zonal wave number and frequency space.

5.2. Implications of Spatial Resolution

The comparison of coSLAM-xc with hiSLAM allows for the investigation of the implications of increasing the grid spacing from 20 km, a grid spacing representative of a high resolution global circulation model, to 2.5 km, a resolution representative of future global circulation models or current weather forecasting models. We find that the representation of convection is qualitatively consistent. In the low-resolution model (coSLAM-xc) updraft velocities lack magnitude and variance, but thermodynamically convection is very similar to the high-resolution models (hiSLAM and NARVAL2; see Figures 6 and 7). In addition, the vertical gravity wave modes of coSLAM-xc and hiSLAM (see Figures 11f and 12) have an almost equal vertical scale. The spectral analyses further show that, at the scales commonly resolved, both models have a comparable zonal momentum flux variance in the stratosphere (see Figures 10a and 10b). However, at scales that are exclusively resolved by hiSLAM and NARVAL2, there is still a large amount of zonal momentum flux variance; the spectral slope, as derived from NARVAL2, is almost flat ($\sim k^{-1}$) until scales at which numerical diffusion sets in. Thus, the potential gravity wave forcing still increases significantly with increasing numerical resolution. As shown in Table 3, the absolute momentum flux of scales shorter than 1,000 km is 10 times greater in hiSLAM than in coSLAM-xc. This comparison, due to the unrealistically flat slope of hiSLAM, has to be interpreted carefully. Still also NARVAL2 resolves almost an order of magnitude more absolute momentum flux and thus we conclude that the grid spacing has a great effect onto the generation of gravity waves by convection. The numerical resolution at which nonorographic gravity wave parameterizations become obsolete can not be anticipated from this work. Insight into this can be found in Preusse et al. (2008). They find that gravity waves with wavelengths shorter than 10 km are removed by vertical reflection and evanescence at their source and more prone to critical level removal. The processes of wave mean-flow interaction, such as wave breaking and dissipation, that drive circulations in the middle atmosphere involve motions of smaller scales that require even finer numerical resolution.

Still it is evident that for the representation of gravity waves in the middle atmosphere also the vertical resolution (see also Watanabe et al., 2015) and the ratio of vertical to horizontal resolution matters. In our tests of one-dimensional spectra of zonal velocity against proposed spectra derived from analytical gravity wave models (see Figures 10c, 10d, 12a), we for hiSLAM and coSLAM-xc find opposite results: coSLAM-xc reproduces the proposed spectral slopes for zonal wave number and frequency space, while hiSLAM reproduces those in vertical wave number space. This result suggests that the fine horizontal resolution of hiSLAM would require a greater vertical resolution. An additional experiment of hiSLAM was conducted on a vertical grid with twice the number of levels. It showed no significant differences and so we perceive hiSLAM's' vertical resolution sufficiently fine. On the other hand the vertical wave number spectra of hiSLAM (see Figure 12) show, that a high horizontal resolution helps to resolve gravity waves also with shorter vertical scales and to reach saturation for scales shorter than the dominant wavelength.

5.3. Implications of a Parameterization of Convection

The spectra of zonal momentum flux in the stratosphere, presented in Figures 10a and 10b, show that in coSLAM-pc, the only experiment using a parameterization of convection, the zonal momentum flux caused by CGGWs is weaker by an order of magnitude at smaller wavelengths and higher frequencies than in coSLAM-xc. We find an analogy to this in a spectrum of precipitation (see Figure 9a), representative for the latent heating and as such for the thermal forcing of gravity waves through convection. The dynamical representation of convection given through the statistics of in-cloud vertical velocities is also inhibited and the variance of upper-tropospheric vertical velocity weakened (see Figures 6d and 9b). For these reasons we find that both, the thermal, and as a consequence also the dynamical forcing of gravity waves, is reduced through a parameterization of convection. As a consequence the forcing of CGGWs onto the mean flow must be expected to be also reduced when using a parameterization of convection. We for these reasons suggest that simulations with a parameterization of convection particularly require a gravity wave drag parameterization.

In vertical wave number spectra of gravity wave properties, shown in Figure 12, we find that coSLAM-pc lacks variance at large vertical scales. This is in agreement with the distribution of heating depths, shown in Figure 5b, which shows that a deep mode in latent heating is missing for coSLAM-pc. This is true even though cloud fraction indicates the presence of deep convection, as can be seen in Figure 5a.

5.4. Implications of SLAMs' Idealized Boundary Conditions

The idealizations of SLAMs are foremost the prescribed SSTs, with its steep meridional gradient, and the absence of planetary rotation. In hiSLAM (as in all SLAMs) the cloud cluster is persistently organized by the prescribed SSTs and for this reasons appears more intense than the convection within the ITCZ, as seen in NARVAL2. As shown in section 3.2 we find greater variability in vertical velocity and temperature anomalies at cloud tops in hiSLAM than in NARVAL2, indicating oscillations at cloud tops. Thus we propose that the flatness of hiSLAM's zonal wave number and frequency spectra is caused by enhanced mechanical forcing through overshooting convective updrafts.

Another factor may be planetary rotation. Horizontal wave number spectra in a rotating framework are generally steeper, meaning that rotation enhances the downscale cascade of energy. However, as NARVAL2 and ICSOM1 reproduce the universal gravity wave spectrum well, we find that planetary rotation in the equatorial region does hardly affect the gravity wave spectrum.

5.5. On Convective Gravity Wave Generation Mechanisms

The generation of gravity waves through tropical convection mainly occurs as a consequence of the release of latent heat, a thermal forcing, or the vertical motion below a stably stratified fluid, a mechanical forcing.

For coSLAM-pc we see that a reduction of gravity wave momentum flux variance (compared to coSLAM-xc), occurs alongside a reduction in variance of precipitation and consequently latent heating, at the same scales. This suggests that the parameterization of convection affects gravity wave generation by misrepresenting small scale variance in latent heating. The latent heating in coSLAM-pc is also limited in its vertical scale and in consistency with that deep modes of gravity waves are inhibited.

For the NARVAL2 and in particular for hiSLAM, we can identify oscillations at cloud tops in probability distributions of vertical velocity and temperature anomalies in clouds (Figures 6 and 7). These oscillations occur below a stably stratified layer, the tropopause, so the mechanical forcing of gravity waves is expected. Further, when looking at the zonal wave number spectra of precipitation and vertical velocity, shown in Figure 9, we see normal behavior in precipitation, representative for the latent heating. However, we find that vertical velocity variance is flat and intense, meaning that the translation of heating into vertical motion is occurring more efficiently in hiSLAM than in other models. For that reason hiSLAM's excess of variance of gravity wave properties in the stratosphere at small scales may phenomenologically be attributed to a mechanical forcing of gravity waves.

6. Conclusions

In this work we present the analysis of gravity waves generated by convective clouds in several models of tropical dynamics. We show that the spectrum of stratospheric zonal momentum flux in zonal wavenumber space is almost flat, with a slope $\sim k^{-1}$, as derived from the realistic high-resolution simulation NARVAL2. The idealized model hiSLAM suggests that an even flatter spectral slope may locally be possible. In an organized convective system, the mechanical generation of gravity waves through convection is enhanced and reflected in the generation of small scale gravity waves. Thus, the representation of CGGWs in atmospheric models requires either fine grid spacing or a gravity wave drag parameterization, as still a significant amount of wave forcing is contained at small scales and high frequencies.

We find that a convective parameterization inhibits gravity wave generation by convective clouds. This is found to be caused by a lack of variance in latent heating at small horizontal scales. Further, although deep convection and high clouds are present, the heating depth is generally diminished in coSLAM-pc. As a consequence no deep gravity wave mode exists and gravity wave variance is reduced for deeper vertical scales. Furthermore, the mechanical generation of gravity waves appears to be inhibited. Thus, the choice of a convective parameterization must be carefully considered when modeling wave-driven circulations in the middle atmosphere. For this reason we advise to turn off a parameterization of convection for simulations with grid spacings of 20 km or less.

NARVAL2 and ICSOM1 show that the universal gravity wave spectrum is realized in realistic simulations of tropical dynamics, as all proposed spectral slopes of one-dimensional spectra of gravity wave properties are reproduced.

Acknowledgments

This research was funded by the Max Planck Institute for Meteorology and the Japan Agency for Marine-Earth Science and Technology, and partly supported by JST CREST Grant JPMJCR1663 (KS), Japan. Computations were carried out at the German Climate Computing Center / Deutsche Klimarechenzentrum (DKRZ) on the *Mistral* super computer. Primary data and scripts used in the analysis that may be used for reproducing the authors' work are stored in the DKRZ long term archive and can be obtained at https://cera-www.dkrz.de/WDCC/ui/cerasearch/entry?acronym=DKRZ_LTA_925_ds00001. We would like to thank two anonymous reviewers for their very helpful comments.

References

Alexander, M., & Holton, J. R. (1997). A model study of zonal forcing in the equatorial stratosphere by convectively induced gravity waves. *Journal of the Atmospheric Sciences*, *54*(3), 408–419.

Alexander, M., Holton, J. R., & Durran, D. R. (1995). The gravity wave response above deep convection in a squall line simulation. *Journal of the Atmospheric Sciences*, *52*(12), 2212–2226.

Baldauf, M., Seifert, A., Förstner, J., Majewski, D., Raschendorfer, M., & Reinhardt, T. (2011). Operational convective-scale numerical weather prediction with the COSMO model: Description and sensitivities. *Monthly Weather Review*, *139*(12), 3887–3905.

Baldwin, M., Gray, L., Dunkerton, T., Hamilton, K., Haynes, P., Randel, W., et al. (2001). The quasi-biennial oscillation. *Reviews of Geophysics*, *39*(2), 179–229.

Becker, T., Stevens, B., & Hohenegger, C. (2017). Imprint of the convective parameterization and sea-surface temperature on large-scale convective self-aggregation. *Journal of Advances in Modeling Earth Systems*, *9*, 1488–1505. <https://doi.org/10.1002/2016MS000865>

Beres, J. H., Alexander, M. J., & Holton, J. R. (2002). Effects of tropospheric wind shear on the spectrum of convectively generated gravity waves. *Journal of the Atmospheric Sciences*, *59*(11), 1805–1824.

Beres, J. H., Garcia, R. R., Boville, B. A., & Sassi, F. (2005). Implementation of a gravity wave source spectrum parameterization dependent on the properties of convection in the whole atmosphere community climate model (WACCM). *Journal of Geophysical Research*, *110*, D10108. <https://doi.org/10.1029/2004JD005504>

Clark, L., Hall, D., & Coen, L. (1996). Source code documentation for the Clark-Hall Cloud-scale Model Code Version G3CH01.

Clark, T. L., Hauf, T., & Kuettner, J. P. (1986). Convectively forced internal gravity waves: Results from two-dimensional numerical experiments. *Quarterly Journal of the Royal Meteorological Society*, *112*(474), 899–925.

Dewan, E., & Good, R. (1986). Saturation and the “universal” spectrum for vertical profiles of horizontal scalar winds in the atmosphere. *Journal of Geophysical Research*, *91*(D2), 2742–2748.

Fovell, R., Durran, D., & Holton, J. (1992). Numerical simulations of convectively generated stratospheric gravity waves. *Journal of the Atmospheric Sciences*, *49*(16), 1427–1442.

Fritts, D. C., & Alexander, M. J. (2003). Gravity wave dynamics and effects in the middle atmosphere. *Reviews of Geophysics*, *41*(1), 1003. <https://doi.org/10.1029/2001RG000106>

Gage, K., & Nastrom, G. (1985). On the spectrum of atmospheric velocity fluctuations seen by MST/ST radar and their interpretation. *Radio Science*, *20*(6), 1339–1347.

Gage, K., & Nastrom, G. (1986a). Spectrum of atmospheric vertical displacements and spectrum of conservative scalar passive additives due to quasi-horizontal atmospheric motions. *Journal of Geophysical Research*, *91*(D12), 13211–13216.

Gage, K., & Nastrom, G. (1986b). Theoretical interpretation of atmospheric wavenumber spectra of wind and temperature observed by commercial aircraft during GASP. *Journal of the Atmospheric Sciences*, *43*(7), 729–740.

Gardner, C. S., Hostetler, C. A., & Franke, S. J. (1993). Gravity wave models for the horizontal wave number spectra of atmospheric velocity and density fluctuations. *Journal of Geophysical Research*, *98*(D1), 1035–1049.

Garrett, C., & Munk, W. (1972). Space-time scales of internal waves. *Geophysical & Astrophysical Fluid Dynamics*, *3*(1), 225–264.

Garrett, C., & Munk, W. (1975). Space-time scales of internal waves: A progress report. *Journal of Geophysical Research*, *80*(3), 291–297.

Hayashi, Y. (1971). A generalized method of resolving disturbances into progressive and retrogressive waves by space Fourier and time cross-spectral analyses. *Journal of the Meteorological Society of Japan*, *49*, 125–128.

Hines, C. O. (1991). The saturation of gravity waves in the middle atmosphere. Part II: Development of doppler-spread theory. *Journal of the Atmospheric Sciences*, *48*(11), 1361–1379.

Holt, L. A., Alexander, M. J., Coy, L., Molod, A., Putman, W., & Pawson, S. (2016). Tropical waves and the quasi-biennial oscillation in a 7-km global climate simulation. *Journal of the Atmospheric Sciences*, *73*(9), 3771–3783.

Holton, J. R. (1973). On the frequency distribution of atmospheric kelvin waves. *Journal of the Atmospheric Sciences*, *30*(3), 499–501.

Holton, J., Beres, J., & Zhou, X. (2002). On the vertical scale of gravity waves excited by localized thermal forcing. *Journal of the Atmospheric Sciences*, *59*(12), 2019–2023.

Johnson, R. H., Rickenbach, T. M., Rutledge, S. A., Ciesielski, P. E., & Schubert, W. H. (1999). Trimodal characteristics of tropical convection. *Journal of Climate*, *12*(8), 2397–2418.

Khairoutdinov, M. F., Krueger, S. K., Moeng, C.-H., Bogenschutz, P. A., & Randall, D. A. (2009). Large-eddy simulation of maritime deep tropical convection. *Journal of Advances in Modeling Earth Systems*, *1*, 15. <https://doi.org/10.3894/JAMES.2009.1.15>

Klemp, J., Dudhia, J., & Hassiotis, A. (2008). An upper gravity-wave absorbing layer for NWP applications. *Monthly Weather Review*, *136*(10), 3987–4004.

Klocke, D., Brueck, M., Hohenegger, C., & Stevens, B. (2017). Rediscovery of the doldrums in storm-resolving simulations over the tropical Atlantic. *Nature Geoscience*, *10*(12), 891.

Koshyk, J. N., & Hamilton, K. (2001). The horizontal kinetic energy spectrum and spectral budget simulated by a high-resolution troposphere–stratosphere–mesosphere GCM. *Journal of the Atmospheric Sciences*, *58*(4), 329–348.

Kraichnan, R. H. (1967). Inertial ranges in two-dimensional turbulence. *The Physics of Fluids*, *10*(7), 1417–1423.

Lane, T. P., & Kniviel, J. C. (2005). Some effects of model resolution on simulated gravity waves generated by deep, mesoscale convection. *Journal of the Atmospheric Sciences*, *62*(9), 3408–3419.

Lane, T. P., & Moncrieff, M. W. (2008). Stratospheric gravity waves generated by multiscale tropical convection. *Journal of the Atmospheric Sciences*, *65*(8), 2598–2614.

Lane, T. P., Reeder, M. J., & Clark, T. L. (2001). Numerical modeling of gravity wave generation by deep tropical convection. *Journal of the Atmospheric Sciences*, *58*(10), 1249–1274.

Liu, H.-L., McInerney, J., Santos, S., Lauritzen, P., Taylor, M., & Pedatella, N. (2014). Gravity waves simulated by high-resolution whole atmosphere community climate model. *Geophysical Research Letters*, *41*, 9106–9112. <https://doi.org/10.1002/2014GL024668>

McLandress, C., Alexander, M. J., & Wu, D. L. (2000). Microwave limb sounder observations of gravity waves in the stratosphere: A climatology and interpretation. *Journal of Geophysical Research*, *105*(D9), 11,947–11,967.

Mellor, G. L., & Yamada, T. (1982). Development of a turbulence closure model for geophysical fluid problems. *Reviews of Geophysics*, *20*(4), 851–875.

Nakanishi, M., & Niino, H. (2006). An improved mellor–yamada level-3 model: Its numerical stability and application to a regional prediction of advection fog. *Boundary-Layer Meteorology*, *119*(2), 397–407.

Nastrom, G., Gage, K., & Jasperson, W. (1984). Kinetic energy spectrum of large-and mesoscale atmospheric processes. *Nature*, *310*(5972), 36–38.

Neale, R. B., & Hoskins, B. (2000a). A standard test for AGCMs including their physical parametrizations. II: Results for the met office model. *Atmospheric Science Letters*, *1*(2), 108–114.

- Neale, R. B., & Hoskins, B. J. (2000b). A standard test for AGCMs including their physical parametrizations: I: The proposal. *Atmospheric Science Letters*, 1(2), 101–107.
- Noda, A. T., Oouchi, K., Satoh, M., Tomita, H., Iga, S.-i., & Tsushima, Y. (2010). Importance of the subgrid-scale turbulent moist process: Cloud distribution in global cloud-resolving simulations. *Atmospheric Research*, 96(2-3), 208–217.
- Nordeng, T. E. (1994). Extended versions of the convective parameterization scheme at ECMWF and their impact on the mean and transient activity of the model in the tropics (Tech. Rep. ECMWF, 206). Shinfield Park, Reading: ECMWF.
- Orr, A., Bechtold, P., Scinocca, J., Ern, M., & Janiskova, M. (2010). Improved middle atmosphere climate and forecasts in the ECMWF model through a nonorographic gravity wave drag parameterization. *Journal of Climate*, 23(22), 5905–5926.
- Piani, C., & Durran, D. (2001). A numerical study of stratospheric gravity waves triggered by squall lines observed during the TOGA COARE and COPT-81 experiments. *Journal of the Atmospheric Sciences*, 58(24), 3702–3723.
- Piani, C., Durran, D., Alexander, M., & Holton, J. (2000). A numerical study of three-dimensional gravity waves triggered by deep tropical convection and their role in the dynamics of the QBO. *Journal of the Atmospheric Sciences*, 57(22), 3689–3702.
- Prein, A. F., Langhans, W., Fosser, G., Ferrone, A., Ban, N., Goergen, K., et al. (2015). A review on regional convection-permitting climate modeling: Demonstrations, prospects, and challenges. *Reviews of Geophysics*, 53, 323–361. <https://doi.org/10.1002/2014RG000475>
- Preusse, P., Eckermann, S. D., & Ern, M. (2008). Transparency of the atmosphere to short horizontal wavelength gravity waves. *Journal of Geophysical Research*, 113, D24104. <https://doi.org/10.1029/2007JD009682>
- Reed, K. A., & Medeiros, B. (2016). A reduced complexity framework to bridge the gap between AGCMs and cloud-resolving models. *Geophysical Research Letters*, 43, 860–866. <https://doi.org/10.1002/2015GL066713>
- Richter, J. H., Sassi, F., & Garcia, R. R. (2010). Toward a physically based gravity wave source parameterization in a general circulation model. *Journal of the Atmospheric Sciences*, 67(1), 136–156.
- Salby, M. L., & Garcia, R. R. (1987). Transient response to localized episodic heating in the tropics. Part I: Excitation and short-time near-field behavior. *Journal of the Atmospheric Sciences*, 44(2), 458–498.
- Sato, K. (1992). Vertical wind disturbances in the afternoon of mid-summer revealed by the MU radar. *Geophysical Research Letters*, 19(19), 1943–1946.
- Sato, K., & Dunkerton, T. J. (1997). Estimates of momentum flux associated with equatorial kelvin and gravity waves. *Journal of Geophysical Research*, 102(D22), 26,247–26,261.
- Sato, K., & Yamada, M. (1994). Vertical structure of atmospheric gravity waves revealed by the wavelet analysis. *Journal of Geophysical Research*, 99(D10), 20,623–20,631.
- Satoh, M., Matsuno, T., Tomita, H., Miura, H., Nasuno, T., & Iga, S.-i. (2008). Nonhydrostatic icosahedral atmospheric model (NICAM) for global cloud resolving simulations. *Journal of Computational Physics*, 227(7), 3486–3514.
- Satoh, M., Tomita, H., Yashiro, H., Miura, H., Kodama, C., Seiki, T., et al. (2014). The non-hydrostatic icosahedral atmospheric model: Description and development. *Progress in Earth and Planetary Science*, 1(1), 18.
- Smith, S. A., Fritts, D. C., & VanZandt, T. E. (1985). Comparison of mesospheric wind spectra with a gravity wave model. *Radio Science*, 20(6), 1331–1338.
- Smith, S. A., Fritts, D. C., & VanZandt, T. E. (1987). Evidence for a saturated spectrum of atmospheric gravity waves. *Journal of the Atmospheric Sciences*, 44(10), 1404–1410.
- Song, I.-S., Chun, H.-Y., & Lane, T. P. (2003). Generation mechanisms of convectively forced internal gravity waves and their propagation to the stratosphere. *Journal of the Atmospheric Sciences*, 60(16), 1960–1980.
- Stephan, C., & Alexander, M. J. (2014). Summer season squall-line simulations: Sensitivity of gravity waves to physics parameterization and implications for their parameterization in global climate models. *Journal of the Atmospheric Sciences*, 71(9), 3376–3391.
- Stevens, B., Giorgetta, M., Esch, M., Mauritsen, T., Crueger, T., Rast, S., et al. (2013). Atmospheric component of the MPI-M earth system model: ECHAM6. *Journal of Advances in Modeling Earth Systems*, 5, 146–172. <https://doi.org/10.1002/jame.20015>
- Tomita, H. (2008). New microphysical schemes with five and six categories by diagnostic generation of cloud ice. *Journal of the Meteorological Society of Japan. Ser. II*, 86, 121–142.
- Tsuda, T., Inoue, T., Kato, S., Fukao, S., Fritts, D., & VanZandt, T. (1989). MST radar observations of a saturated gravity wave spectrum. *Journal of the Atmospheric Sciences*, 46(15), 2440–2447.
- Tsuda, T., Murayama, Y., Wirjosumarto, H., Harijono, S. W. B., & Kato, S. (1994). Radiosonde observations of equatorial atmosphere dynamics over Indonesia: 2. Characteristics of gravity waves. *Journal of Geophysical Research*, 99(D5), 10,507–10,516.
- Warner, C., & McIntyre, M. (1996). On the propagation and dissipation of gravity wave spectra through a realistic middle atmosphere. *Journal of the Atmospheric Sciences*, 53(22), 3213–3235.
- Watanabe, S., Sato, K., Kawatani, Y., & Takahashi, M. (2015). Vertical resolution dependence of gravity wave momentum flux simulated by an atmospheric general circulation model. *Geoscientific Model Development*, 8(6), 1637–1644.
- Weinstock, J. (1985a). Theoretical gravity wave spectrum in the atmosphere: Strong and weak wave interactions. *Radio Science*, 20(6), 1295–1300.
- Weinstock, J. (1985b). On the theory of temperature spectra in a stably stratified fluid. *Journal of Physical Oceanography*, 15(4), 475–477.
- Zängl, G., Reinert, D., Ripodas, P., & Baldauf, M. (2015). The ICON (ICOsahedral non-hydrostatic) modelling framework of DWD and MPI-M: Description of the non-hydrostatic dynamical core. *Quarterly Journal of the Royal Meteorological Society*, 141(687), 563–579.
- Zhang, S. D., Huang, C. M., Huang, K. M., Gong, Y., Chen, G., Gan, Q., & Zhang, Y. H. (2017). Latitudinal and seasonal variations of vertical wave number spectra of three-dimensional winds revealed by radiosonde observations. *Journal of Geophysical Research: Atmospheres*, 122, 13,174–13,190. <https://doi.org/10.1002/2017JD027602>
- Zhang, S. D., Huang, C. M., Huang, K. M., Zhang, Y. H., Gong, Y., & Gan, Q. (2017). Vertical wavenumber spectra of three-dimensional winds revealed by radiosonde observations at midlatitude. *Annales Geophysicae*, 35, 107. Copernicus GmbH.
- Zhao, J., Chu, X., Chen, C., Lu, X., Fong, W., Yu, Z., et al. (2017). Lidar observations of stratospheric gravity waves from 2011 to 2015 at McMurdo (77.84° S, 166.69° E), antarctica: 1. Vertical wavelengths, periods, and frequency and vertical wave number spectra. *Journal of Geophysical Research: Atmospheres*, 122, 5041–5062. <https://doi.org/10.1002/2016JD026368>